



NLR-TP-2014-258

Spectral broadening by shear layers of open jet wind tunnels

AIAA Paper 2014-3178

P. Sijtsma, S. Oerlemans, T.G. Tibbe, T. Berkefeld and C. Spehr

Nationaal Lucht- en Ruimtevaartlaboratorium

National Aerospace Laboratory NLR

Anthony Fokkerweg 2

P.O. Box 90502

1006 BM Amsterdam

The Netherlands

Telephone +31 (0)88 511 31 13

Fax +31 (0)88 511 32 10

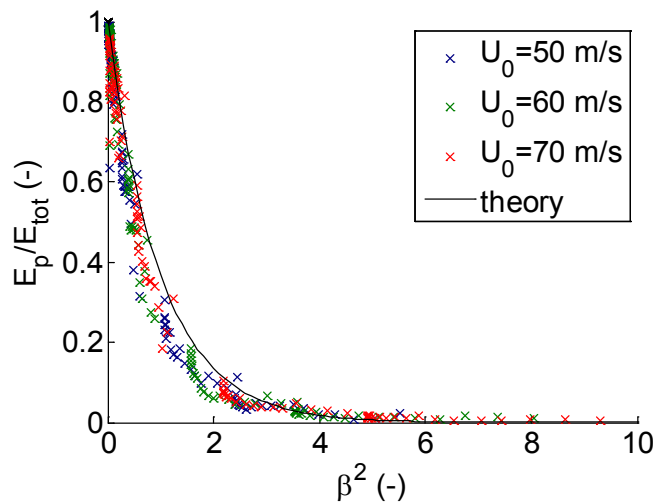
www.nlr.nl



Executive summary

Spectral broadening by shear layers of open jet wind tunnels

AIAA Paper 2014-3178



Report no.

NLR-TP-2014-258

Author(s)

P. Sijtsma
S. Oerlemans
T.G. Tibbe
T. Berkefeld
C. Spehr

Report classification

UNCLASSIFIED

Date

June 2014

Knowledge area(s)

Aëro-akoestisch en experimenteel
aërodynamisch onderzoek

Descriptor(s)

Garteur
Spectral Broadening
Shear Layers
Low Speed Wind Tunnels

Problem area

The presence of shear layers in open jet wind tunnels complicates aeroacoustic measurements. Tones from wind tunnel models are subject to spectral broadening (or 'haystacking') when propagating through the turbulent shear layer flow. For example, in measurements on contra-rotating propellers this obscures the identification and quantification of rotor tones.

Description of work

This paper describes a theoretical and experimental study into spectral broadening by the shear layers of open jet wind tunnels. A simple physical model is derived which

predicts the amount of broadening as a function of a single parameter, which is proportional to wind speed, source frequency and shear layer thickness. The theory is compared against experimental data from five different wind tunnels.

Results and conclusions

Especially for the smaller wind tunnels the agreement between theory and experiment is generally good, which makes it possible to retrieve the original level of a tone from a broadened spectrum.

Applicability

The results of this study can be used to improve the quality of aeroacoustic wind tunnel tests.



NLR-TP-2014-258

Spectral broadening by shear layers of open jet wind tunnels

AIAA Paper 2014-3178

P. Sijtsma, S. Oerlemans¹, T.G. Tibbe², T. Berkefeld³ and C. Spehr³

¹ Siemens Wind Power

² Philips Consumer Lifestyle

³ German Aerospace Center DLR




This report is based on a presentation held at the 20th AIAA/CEAS Aeroacoustics Conference, Atlanta, GA, June 16-20, 2014.

The contents of this report may be cited on condition that full credit is given to NLR and the authors.

This publication has been refereed by the Advisory Committee AEROSPACE VEHICLES.

Customer National Aerospace Laboratory NLR
Contract number -----
Owner NLR
Division NLR Aerospace Vehicles
Distribution Unlimited
Classification of title Unclassified
Date June 2014

Approved by:

Author P. Sijtsma 	Reviewer M. Tuinstra 	Managing department J. Hakkaart 
Date: 12-06-14	Date: 12-06-14	Date: 13/6/14

Summary

The presence of shear layers in open jet wind tunnels complicates aeroacoustic measurements. Tones from wind tunnel models are subject to spectral broadening (or ‘haystacking’) when propagating through the turbulent shear layer flow. For example, in measurements on contra-rotating propellers this obscures the identification and quantification of rotor tones. This paper describes a theoretical and experimental study into spectral broadening by the shear layers of open jet wind tunnels. A simple physical model is derived which predicts the amount of broadening as a function of a single parameter, which is proportional to wind speed, source frequency and shear layer thickness. The theory is compared against experimental data from five different wind tunnels. Especially for the smaller wind tunnels the agreement between theory and experiment is generally good, which makes it possible to retrieve the original level of a tone from a broadened spectrum



This page is intentionally left blank.

Contents

Nomenclature	6
1 Introduction	7
2 Theoretical model	7
2.1 Effect of time delay variations on a tonal signal	7
2.2 Estimation of time delay variations	8
3 Experimental study in DNW-PLST wind tunnel	11
3.1 Wind tunnel	11
3.2 Aerodynamic measurements	11
3.3 Acoustic measurements	12
4 Comparison to other wind tunnels	13
4.1 VKI tunnel	13
4.2 DNW-LLF tunnel	14
4.3 NLR-KAT tunnel	15
4.4 DNW-NWB tunnel	16
5 Conclusions	17
Appendix A The relation between spectral broadening and time delay variations	19
A.1 Some definitions	19
A.2 General expressions	20
A.3 Evaluation of shape function	21
A.4 Summary	23
Acknowledgements	24
References	25

Nomenclature

DNW	German-Dutch Wind tunnels	$p(t)$	acoustic pressure
KAT	Small Anechoic Tunnel	$R_{\varepsilon\varepsilon}(t)$	auto-correlation function of $\varepsilon(t)$
LLF	Large-Low-speed Facility	t	time
NWB	Low-speed Wind tunnel Braunschweig	T_v	maximum lateral turbulence intensity
PLST	Pilot Low-Speed Tunnel	U	axial velocity
VKI	Von Karman Institute	U_0	axial velocity at nozzle exit
$A_{pp}(f)$	auto-spectrum of $p(t)$	\bar{v}	flow velocity
$b(t)$	defined in Eq. (6)	\bar{v}_t	turbulent flow velocity
$B(f)$	Fourier transform of $b(t)$	v_{max}	maximum lateral turbulent velocity
c_0	speed of sound	v_y	lateral turbulent velocity
\bar{e}_x	unit vector in x -direction	x	axial coordinate
E_p	acoustic energy in peak	x_0	virtual shear layer origin
E_{rot}	total acoustic energy in spectrum	\bar{x}_m	position of microphone
f	frequency	x_m	axial position of microphone
f_0	source frequency	\bar{x}_s	position of sound source
$g(t)$	defined below Eq. (2): $g(t) = \exp(2\pi i f_0 \varepsilon(t))$	x_s	axial position of sound source
i	imaginary unit	y	lateral coordinate
l	length scale of shear layer turbulence	y_0	lateral coordinate of shear layer centre
M_0	tunnel Mach number	z	vertical coordinate
α	pressure amplitude	$\varepsilon(t)$	time delay variation
β	broadening constant: $\beta = 2\pi f_0 \varepsilon_{rms}$	$\zeta(\tau)$	defined below Eq. (4): $\zeta(\tau) = \varepsilon(t + \tau) - \varepsilon(\tau)$
δ'	shear layer momentum thickness	θ	propagation angle
δ_{95}	physical shear layer thickness	λ	acoustic wavelength
δ_{CA}	shear layer thickness used by Candel et al	ξ	defined by Eq. (11): $\xi = \sigma y / (x - x_0)$
$\delta(f)$	Dirac delta function	ξ_0	lateral shear layer offset
ΔdB	reduction in peak level (in dB)	σ	shear layer spreading parameter
Δt	average time delay	τ	time
Δf	frequency shift between tone and sidelobe	$\Psi(f)$	shape function

1 Introduction

Aeroacoustic wind tunnel tests are often conducted in open jet wind tunnels. By placing the microphones outside the tunnel flow, flow-induced self-noise on the microphones can be prevented. However, before the sound from the model arrives at the out-of-flow microphones, it has to pass through the open jet shear layer. The effect of the shear layer on the transmitted sound is twofold. First, the sound is refracted due to the change of the mean flow speed across the shear layer. Refraction is well described by the theory of Amiet^{1,2}, which has been validated experimentally several times³⁻⁵. Second, due to turbulence in the shear layer, the transmitted sound is affected by unsteady phase and amplitude distortions. This leads to spectral broadening or ‘haystacking’. For a tonal source this means that part of the acoustic energy is scattered to other frequencies, resulting in a broadband hump around the main spectral peak and a reduced peak level. The characteristics of spectral broadening depend on flow speed, frequency, shear layer thickness, and incidence angle, and are presently only partially understood. As a result they hamper the interpretation of acoustic measurements substantially. For example, in acoustic wind tunnel measurements on contra-rotating propellers, spectral broadening complicates the identification and quantification of rotor tones.

Classical experiments on spectral broadening in an open jet wind tunnel were performed by Candel et al^{6,7} and by Guedel^{8,9}. The broadened spectra typically showed a narrow peak accompanied by two ‘shoulders’ or sidelobes. Comprehensive theoretical studies were carried out by Campos^{10,11} and Cargill¹². More recently, spectral broadening was studied using Computational Aero-Acoustics methods^{13,14} and a weak scattering model^{15,16}. These methods correctly predicted the general trends observed in experiments, but did not yield a simple correction method for shear layer broadening.

This paper describes an experimental and theoretical study into spectral broadening by the shear layers of open jet wind tunnels. The objectives are (1) to determine the experimental broadening characteristics as a function of wind speed, source frequency and shear layer thickness, (2) to investigate whether spectral broadening (loss of energy in a tone) can be predicted using a simple theoretical model, and (3) to determine whether spectral broadening in different wind tunnels has universal characteristics. If the amount of broadening can be predicted, simple scaling rules may be derived to correct out-of-flow measurements for broadening effects. Thus, the original acoustic energy of broadened tones may be retrieved.

The investigations reported in this paper were done within GARTEUR AD/AG-50: “Effect of Open Jet Shear Layers on Aeroacoustic Wind Tunnel Measurements”. A similar investigation, within the same GARTEUR group, was carried out by Kröber et al¹⁷.

The structure of this paper is as follows. In Section II, a simple theoretical model is developed which predicts the characteristics of spectral broadening in terms of time delay variations. Section III describes wind tunnel experiments in which the effects of wind speed, source frequency, and shear layer thickness on spectral broadening are investigated. The scaled experimental results are compared to the theoretical predictions. In Section IV the broadening characteristics of different wind tunnels are compared to each other. The conclusions of this study are summarised in Section V.

2 Theoretical model

This section describes an analytical model that predicts the characteristics of spectral broadening in terms of time delay variations. Based on previous experimental studies^{4,9}, it is assumed that the sound propagation and refraction can be described by ray acoustics, and that the interaction between the acoustic wave and the turbulent flow is limited to the shear layer intersection point. Furthermore, it is assumed that spectral broadening is mainly caused by time delay variations due to shear layer turbulence. This means that amplitude variations are neglected.

In Section II.A a mathematical model is presented to model the effect of time delay variations on a tonal signal. Section II.B describes a simple physical model by which the time delay variations can be estimated.

2.1 Effect of time delay variations on a tonal signal

In this subsection a short summary is given of a more elaborate derivation given in the appendix. Suppose a tonal sound source is placed inside the jet, and its sound is received by a microphone outside the jet. If the emitted sound has frequency f_0 , the microphone receives the signal

$$p(t) = \alpha \exp(2\pi i f_0 (t + \Delta t + \varepsilon(t))), \quad (1)$$

where Δt is the average time delay and $\varepsilon(t)$ the time delay variation. Assuming that the amplitude α is independent of time, it can be shown that the auto-spectrum $A_{pp}(f)$ is given by

$$A_{pp}(f) = \alpha^2 \Psi(f - f_0), \quad (2)$$

where $\Psi(f) = A_{gg}(f)$ is the ‘shape function’, i.e., the auto-spectrum of $g(t) = \exp(2\pi i f_0 \varepsilon(t))$. Since

$$\int_{-\infty}^{\infty} \Psi(f) df = 1, \quad (3)$$

acoustic energy is conserved and

$$p_{\text{rms}}^2 = \int_{-\infty}^{\infty} A_{pp}(f) df = \alpha^2 \int_{-\infty}^{\infty} \Psi(f - f_0) df = \alpha^2. \quad (4)$$

Note that in general the shape function $\Psi(f)$ is not necessarily symmetric around $f = 0$, since $g(t)$ is not real-valued. However, in the following, an approximation is discussed for which $\Psi(f)$ is symmetric nevertheless.

It is assumed that the values of the function $\zeta(\tau) = \varepsilon(t + \tau) - \varepsilon(\tau)$ exhibit a Gaussian probability density function for any value of t . Although there is no physical reason why ζ should be Gaussian (especially for small t), the subsequent analysis may predict some trends which are also valid for non-Gaussian ζ . Under this assumption it can be shown that

$$\Psi(f) = \exp\left(-\left(2\pi f_0 \varepsilon_{\text{rms}}\right)^2\right) \delta(f) + B(f), \quad (5)$$

where $B(f)$ is the Fourier transform of

$$b(t) = \exp\left(-\left(2\pi f_0 \varepsilon_{\text{rms}}\right)^2\right) \left(\exp\left(\left(2\pi f_0\right)^2 R_{\varepsilon\varepsilon}(t)\right) - 1\right), \quad (6)$$

in which $R_{\varepsilon\varepsilon}(t)$ is the auto-correlation function of $\varepsilon(t)$. Since $b(t)$ tends to zero for large values of t , $B(f)$ does not contain a sharp peak. Thus, we see that the shape function $\Psi(f)$ consists of a sharp peak and a broadband contribution. The ratio of the acoustic energy in the peak and the total acoustic energy is given by

$$E_p / E_{\text{tot}} = \exp\left(-\left(2\pi f_0 \varepsilon_{\text{rms}}\right)^2\right), \quad (7)$$

and depends only on the value of $f_0 \varepsilon_{\text{rms}}$.

Without Gaussian assumption, and if $f_0 \varepsilon_{\text{rms}}$ is sufficiently small, it can be derived that

$$E_p / E_{\text{tot}} \approx 1 - \left(2\pi f_0 \varepsilon_{\text{rms}}\right)^2, \quad (8)$$

which is, in first order, the same as Eq. (7).

2.2 Estimation of time delay variations

In the previous subsection it was shown that for both approximations the energy ratio (i.e., the ratio of the acoustic energy in the peak and the total acoustic energy) only depends on the value of $f_0 \varepsilon_{\text{rms}}$. Thus, the original acoustic energy of a tone in a broadened spectrum can be retrieved if a reliable estimate of ε_{rms} is available. The *shape* of the broadened spectrum was shown to depend on the frequency content of $\varepsilon(t)$. The present subsection describes a simple physical model by which the time delay variations can be estimated. This model will be verified against experiments in subsequent sections.

Shear layer thickness

First, an estimate for the thickness of the shear layer is determined. Assuming self-similarity, Görtler¹⁸ derived the following expression for the mean axial velocity distribution U in a plane free shear layer:

$$\frac{U}{U_0} = \frac{1}{2} [1 + \operatorname{erf}(\xi + \xi_0)], \quad (9)$$

where U_0 is the axial velocity at the nozzle exit. The error function is defined by

$$\operatorname{erf}(\xi) = \frac{2}{\sqrt{\pi}} \int_0^{\xi} e^{-\zeta^2} d\zeta. \quad (10)$$

Furthermore, we have

$$\xi = \frac{\sigma y}{x - x_0}, \quad (11)$$

with x and y the axial and the lateral coordinate, respectively. The starting point of the shear layer development is given by $x = x_0$, which can be at the nozzle exit or upstream. For the lateral offset ξ_0 and the spreading parameter σ empirical values are available¹⁹⁻²¹:

$$\begin{cases} 9 \leq \sigma \leq 13.5, \\ \xi_0 \approx 0.3. \end{cases} \quad (12)$$

The momentum thickness is given by

$$\delta' = \int_{-\infty}^{\infty} \frac{U(y)}{U_0} \left(1 - \frac{U(y)}{U_0}\right) dy \quad (13)$$

This can be elaborated²³ as

$$\delta' = \frac{x - x_0}{2\sigma} \int_0^{\infty} [1 + \operatorname{erf}(\xi)] (1 - \operatorname{erf}(\xi)) d\xi = \frac{x - x_0}{\sigma\sqrt{2\pi}} \quad (14)$$

Other shear layer thickness definitions

The “physical” shear layer thickness is defined as the difference between the y -values in between which U varies from $0.05U_0$ to $0.95U_0$. It can be shown that

$$\delta_{95} \approx 5.83\delta'. \quad (15)$$

Candel et al^{6,7} and McAlpine¹⁵ use a thickness definition δ_{CA} based on a different shear layer distribution:

$$\frac{U}{U_0} = \frac{1}{2} \left[1 + \tanh\left(\frac{2}{\delta_{CA}}(y - y_0)\right) \right]. \quad (16)$$

It can be shown numerically that

$$\delta_{95} = 1.47\delta_{CA} \quad (17)$$

Hence,

$$\delta_{CA} = \frac{\delta_{95}}{1.47} = 4.0\delta' \quad (18)$$

Candel's estimate for the thickness development is

$$\delta_{CA} = 0.17(x - x_0). \quad (19)$$

Comparing this with (18) and (14), we obtain

$$\sigma = \frac{4.0}{0.17\sqrt{2\pi}} = 9.4, \quad (20)$$

which is within the range mentioned in Eq. (12).

Approximation of time delay variation

Let the total flow velocity be written as

$$\bar{v} = U\bar{e}_x + \bar{v}_t, \quad (21)$$

where \bar{U} is the time-averaged velocity and \bar{v}_t the turbulent velocity in the shear layer. A first estimate for the time delay variation between an acoustic source at \bar{x}_s and a microphone at \bar{x}_m is the contour integral

$$\varepsilon(t) = \frac{1}{c_0^2} \int \bar{v}_t \cdot d\bar{s}, \quad (22)$$

in which c_0 is the sound speed, and where \bar{s} follows the acoustic ray between \bar{x}_s and \bar{x}_m . If the fluctuation of \bar{v}_t in the x -direction is sufficiently slow, Eq. (22) can be approximated by

$$\varepsilon(t) = \frac{1}{c_0^2} \int_{-\infty}^{\infty} v_y dy, \quad (23)$$

where v_y is the lateral component of the turbulent velocity. Now we postulate:

$$v_y(x, y, t) = v_y(x, y_0, t) \exp\left[-(\xi + \xi_0)^2\right]. \quad (24)$$

This is a reasonable assumption at locations where the shear layer is basically a vortex train. Then we can evaluate (23) as

$$\varepsilon(t) = \frac{v_y(x, y_0, t)}{c_0^2} \int_{-\infty}^{\infty} \exp\left[-(\xi + \xi_0)^2\right] dy. \quad (25)$$

Herein, we have

$$\int_{-\infty}^{\infty} \exp\left[-(\xi + \xi_0)^2\right] dy = \frac{(x - x_0)}{\sigma} \int_{-\infty}^{\infty} \exp(-\xi^2) d\xi = \frac{(x - x_0)\sqrt{\pi}}{\sigma} = \pi\sqrt{2}\delta'. \quad (26)$$

Hence,

$$\varepsilon_{\text{rms}} = \frac{v_{\text{max}}(x - x_0)\sqrt{\pi}}{c_0^2 \sigma} = \frac{\pi\sqrt{2}v_{\text{max}}\delta'}{c_0^2}, \quad (27)$$

where v_{max} is the rms-value of the lateral turbulent velocity at the centre of the shear layer.

Turbulence properties

The ratio T_v between v_{max} and U_0 is usually independent of the axial distance $x - x_0$. Previous experimental studies^{3,20,21} reported values between 0.11 and 0.14. Herewith, we can write for (27):

$$\varepsilon_{\text{rms}} = \frac{T_v U_0 (x - x_0)\sqrt{\pi}}{c_0^2 \sigma} = \frac{\pi\sqrt{2}T_v U_0 \delta'}{c_0^2}, \quad (28)$$

Inserting (28) into Eq. (7) gives

$$E_p / E_{\text{tot}} = \exp(-\beta^2), \quad (29)$$

with the dimensionless parameter β given by

$$\beta = \frac{2\pi\sqrt{\pi}T_v}{\sigma c_0^2} f_0 U_0 (x - x_0) = \frac{2\sqrt{2}\pi^2 T_v f_0 U_0 \delta'}{c_0^2}. \quad (30)$$

Thus, within the present approximation, the amount of broadening for a shear layer with given T_v and σ only depends on the value of $f_0(x - x_0)U_0$. Rearranging Eq. (30) in dimensionless groups yields

$\beta = 2\pi\sqrt{2}\pi T_v M_0 \delta' / \lambda$, which clearly indicates the relevant parameters: the turbulence intensity in the shear layer, the Mach number of the tunnel flow, and the ratio of shear layer thickness and acoustic wave length¹⁷. Note that Guedel⁹ obtained an expression similar to Eq. (8) using a different approach.

Sidelobe peaks

Eq. (62) in the appendix shows that for small $f_0 \varepsilon_{\text{rms}}$ the shape of the broadened spectrum is determined by the spectrum of $\varepsilon(t)$. The dominant frequency of the time delay variations, which determines the frequency shift Δf

between the tone and the side-lobes in the broadened spectrum, can be estimated as the frequency at which a train of vortices passes a certain point in the shear layer:

$$\Delta f \approx \frac{0.5U_0}{l}, \quad (31)$$

where l is a length scale of the shear layer turbulence. Candel et al⁶ proposed the estimates $U_c = \frac{1}{2}U_0$ and $l = 3.2\delta_{CA}$. McAlpine¹⁵ found the following relation:

$$\Delta f = \frac{1}{\pi\sqrt{2}} \frac{0.5U_0}{l} \quad (32)$$

The proposed relation with the shear layer thickness was

$$l = \delta_{CA}. \quad (33)$$

Consequently:

$$\Delta f = \frac{0.5U_0}{4.4\delta_{CA}}. \quad (34)$$

Thus, the side-lobes are expected to move outward with increasing tunnel speed and decreasing shear layer thickness. Moreover, Δf is expected to be independent of frequency.

3 Experimental study in DNW-PLST wind tunnel

This section describes an experimental study into spectral broadening by the open jet of the DNW-PLST wind tunnel. First, the wind tunnel is described in Section III.A. Then the aerodynamic measurements and their results are discussed in Section III.B. The acoustic experiments are described and analysed in Section III.C.

3.1 Wind tunnel

The experiments were carried out in the open jet of the DNW-PLST wind tunnel (Figure 1), which is a 1:10 scale model of the DNW-LLF wind tunnel. The nozzle has a width of 0.8 m and a height of 0.6 m. The maximum flow speed is 80 m/s, but to avoid heating of the tunnel most tests were done at 20, 40, and 60 m/s. The wind tunnel speed was controlled using a Pitot-static tube inside the open jet. All aerodynamic and acoustic measurements were done on the vertical shear layer at $y = 0$. On the opposite side of the nozzle, an optional nozzle extension plate was mounted ($1.2 \times 0.8 \text{ m}^2$). This plate was used to install the calibration source for the acoustic measurements. By comparing hotwire results with and without this extension plate, it was verified that the plate had no effect on the shear layer at $y = 0$ (within the measurement accuracy). In earlier tests it was verified that spectral broadening by the boundary layer over the extension plate was negligible compared to the broadening by the shear layer. To investigate the effect of increased shear layer thickness, the nozzle boundary layer could be tripped using three 16-mm diameter PVC tubes mounted at the tunnel wall upstream of the nozzle exit.

3.2 Aerodynamic measurements

The aerodynamic measurements were done by traversing a cross-wire horizontally through the shear layer, at tunnel axis height and at three axial stations: $x = 0.35 \text{ m}$, $x = 0.70 \text{ m}$, and $x = 1.30 \text{ m}$. The second axial station corresponds to the standard model position, the third station was the most downstream position that was attainable in the present set-up. The two hotwires were placed in the horizontal plane, both oriented at an angle of 45° with the tunnel axis. In this way, the unsteady velocities in the horizontal plane could be measured.

The normalised mean axial velocity profiles at the three axial stations are shown in Figure 2. It can be seen that the shear layer flow is self-similar for both the reference and the tripped nozzle. The profiles match the Görtler solution from Eq. (9) with $\sigma = 11$ and $\xi_0 = 0.32$, well in line with the literature values mentioned in Eq. (12). The

effect of the nozzle trip is to move the virtual origin upstream by 0.37 m. Using these values for σ and x_0 , the physical shear layer thickness for given x can be determined with Eqs. (14) and (15).

The turbulence intensity profiles at the three axial stations are shown in Figure 3. Although there are small variations, the turbulence profiles are generally self-similar. The maximum turbulence intensity occurs at the centre of the shear layer, with values of about 17% and 13% for the axial and lateral turbulence, respectively. These values correspond well to the literature values mentioned above Eq. (28). For the two upstream axial stations, the tripped nozzle exhibits slightly higher turbulence intensities than the reference nozzle. Note that the spectral shapes of the lateral turbulence agree with the assumption made in Eq. (24).

The turbulence spectra (Figure 4) have a broadband character without tonal components, indicating the absence of periodic vortex shedding. The low-frequency content of the turbulence can be seen to increase with increasing axial distance, due to the larger turbulence length scale.

The effect of wind speed on the flow parameters is shown in Figure 5. The mean velocity and turbulence intensity profiles are practically identical for the two higher wind speeds, but the 20 m/s results show a slightly higher turbulence intensity. This atypical behaviour at the lowest speed, which is also visible in the turbulence spectra, is attributed to transitional effects inside the wind tunnel nozzle. In the next subsection it will be shown that these differences in flow characteristics are also visible in the acoustic results.

3.3 Acoustic measurements

For the acoustic measurements, the floor, ceiling and walls of the test section were treated with foam to suppress acoustic reflections. A speaker (1" BMS compression driver) was installed slightly recessed in the nozzle extension plate, at tunnel axis height and two axial positions: $x_s = 0.35$ m and $x_s = 0.70$ m (Figure 1). The speaker produced tonal noise with frequencies between 4 kHz and 30 kHz. Outside the shear layer eight ½" LinearX M51 microphones (with wind screen) were placed at tunnel axis height and axial positions x_m between 0.175 m and 1.475 m. The acoustic data were acquired at a sample rate of 102.4 kHz and a measurement time of 20 s. The data were processed using an FFT block size of 65536 and a Hanning window with 50% overlap, yielding 61 averages and a frequency resolution of 1.56 Hz. All data were corrected for wind tunnel background noise and data with a signal-to-noise ratio less than 3 dB were discarded.

The effect of wind speed on spectral broadening is shown in Figure 6 for the reference nozzle. Since $x_m = x_s$, the sound passes the shear layer almost normally. In order to account for possible variations in source strength, all spectra were normalised using the peak SPL in the spectra. The broadened spectra show a narrow peak surrounded by two sidelobes, as observed previously by Candel et al⁷. The energy in the sidelobes increases with wind speed, as expected on the basis of Eq. (29): β increases with U_0 , which gives a decrease in E_p/E_{tot} . Furthermore, the frequency shift between peak and sidelobe, Δf , increases more or less linearly with increasing wind speed, as expected on the basis of Eq. (31). Using $\Delta f \approx 70$ Hz and $U_0 = 60$ m/s, and calculating δ_{CA} from Eqs. (18) and (14) with $\sigma = 11$ (as determined in the previous subsection), we find $l/\delta_{CA} = 0.5U_0/\delta_{CA}\Delta f \approx 4.2$, which is in between the values of 3.2 and 4.4 suggested by Candel et al⁷ and McAlpine et al¹⁵, respectively (see Eqs. (31) and (34)).

The effect of frequency on spectral broadening is shown in Figure 7 for the reference nozzle. Note that due to background noise the frequency range is limited for the lowest source frequencies. The sharp peaks at $\Delta f = \pm 200$ Hz are most probably related to a 200 Hz peak in the background noise spectrum, and not to the shear layer. In line with Eqs. (7) and (31), the broadband energy increases with frequency, and Δf does not depend on the peak frequency f_0 .

The effect of shear layer thickness on spectral broadening is shown in Figure 8. The thickness was increased by (1) increasing the source (and microphone) axial position, and (2) tripping the nozzle. As expected on the basis of Eqs. (7) and (31), the broadband energy increases with increasing shear layer thickness, while Δf decreases. Interestingly, the spectra for the reference nozzle at $x_s = 0.70$ m and the tripped nozzle at $x_s = 0.35$ m nearly coincide. This is in line with the observation in the previous subsection that the effect of the nozzle trip is to move the virtual origin upstream by 0.37 m. Finally, Figure 9 shows the spectra at all microphones for the reference nozzle and a fixed source position of $x_s = 0.70$ m (oblique passage of the sound through the shear layer). Due to the

increasing shear layer thickness with increasing axial distance, the broadband energy increases and Δf decreases with increasing microphone number.

In order to verify Eq. (29) quantitatively, the energy ratio E_p/E_{tot} was determined from the experiments. E_p was calculated by integrating the acoustic energy between the two local minima around the peak (the minima were found by smoothing the spectra using a 4-point moving average). For E_{tot} all energy within ± 2000 Hz of the peak was integrated (not the whole spectrum to avoid inclusion of higher harmonics). The value of β was determined from Eq. (30) with $\sigma = 11$ and $T_v = 0.13$ (as determined from the hotwire measurements described in the previous subsection). Figure 10 shows the results for all measurements with $x_m = x_s$ (normal incidence), i.e., for three wind speeds, reference and tripped nozzle, two source positions, and five source frequencies (4 kHz was discarded due to limited signal-to-noise ratio, see Figure 7). Interestingly, practically all results collapse on a single curve, indicating that the amount of broadening depends only on the dimensionless parameter β . Moreover, the experimental results are close to the theoretical curve, providing substantial support for the theoretical model described in Section II. This is quite remarkable in view of the simplifications made in the derivation of the model. The largest deviations from the theoretical curve are observed for the measurements with the untripped nozzle at 20 m/s. This is attributed to the differences in flow characteristics for these conditions (due to transitional effects inside the wind tunnel nozzle), as described in the previous subsection.

Figure 11 shows the results for all measurements and all microphones, including those with $x_m \neq x_s$. For the current measurements, the propagation angle θ with respect to the downstream direction, as defined by Amiet¹, varied between about 55° and 109° . It can be seen that all measurements roughly follow the same curve, except the measurements with the untripped nozzle at 20 m/s as discussed above.

The experimental results indicate that, at least for this wind tunnel, the energy of a broadened tone, for given $f_0(x-x_0)U_0$, can be retrieved by calculating β from Eq. (30) and reading the corresponding energy ratio from the experimental curve in Figure 11. The reduction in peak level (in dB) due to spectral broadening then simply follows from $\Delta \text{dB} = 10 \log(E_p/E_{tot})$. For example, energy ratios of 0.5, 0.25, and 0.1 correspond to reductions in peak level of 3 dB, 6 dB, and 10 dB, respectively. In the next section it will be investigated whether other wind tunnels also exhibit a univocal relation between β and energy ratio, and if so, if this relation is the same for different wind tunnels.

4 Comparison to other wind tunnels

In the previous section it was shown that for the DNW-PLST wind tunnel the amount of spectral broadening (energy loss of a tone) only depends on the value of the dimensionless broadening parameter β , which can be simply determined from the tone frequency, the tunnel speed, and the axial positions of the source and the microphone. Thus, as long as the tone can be recognized in the broadened spectrum, the original tone level can be retrieved. In the present section it will be investigated if other wind tunnels exhibit the same relation between β and energy ratio. This analysis is carried out for the following open jet wind tunnels:

- the VKI tunnel used in the classical experiments by Candel et al⁶⁻⁹, which has a round jet with a diameter of 3 m;
- the DNW-LLF wind tunnel, with a 6×6 m² square nozzle;
- the NLR-KAT wind tunnel, which has a 0.4×0.5 m² rectangular nozzle;
- the DNW-NWB wind tunnel, which has a 3.25×2.8 m² rectangular nozzle.

4.1 VKI tunnel

The VKI tunnel has a circular nozzle with a diameter of 3 m. Aerodynamic measurements⁶ show that the shear layer spreading parameter σ for this jet is about 11 and the maximum lateral turbulence intensity T_v about 0.12. Using a tonal noise source on the tunnel axis, spectral broadening was measured for several source positions, wind speeds and source frequencies. In Fig. 5 of Guedel's paper⁹ the energy ratio $1 - E_p/E_{tot}$ is plotted for an axial source position of 1.95 m, tunnel speeds U_0 of 20, 40, and 57 m/s, and source frequencies of 4, 6, 8, 10, 12, 15,

20 kHz. These data are plotted as a function of the dimensionless parameter β in Figure 12. Although some scatter occurs, the data follow the theoretical curve quite well. Thus, the normalised spectral broadening behaviour of the VKI tunnel is similar to that of the DNW-PLST, and both follow the trend predicted by the simple physical model from Section II.

4.2 DNW-LLF tunnel

The acoustic measurements in the DNW-LLF were done using the $6 \times 6 \text{ m}^2$ square nozzle with an extension plate. The test set-up was similar to the PLST set-up shown in Figure 1. The test hall was treated with foam to suppress acoustic reflections. A speaker (1" BMS compression driver) was installed in the nozzle extension plate, at tunnel axis height and 4.4 m downstream of the nozzle. The speaker produced tonal noise with frequencies of 1, 2, 4, 8, 16, 20 and 25 kHz, and measurements were taken at wind speeds of 62 m/s and 77 m/s. Outside the opposite shear layer an axial row of farfield microphones was placed at tunnel axis height and a lateral distance of 16 m to the tunnel axis. It should be noted that between the source and some of the farfield microphones a phased array consisting of microphones in an acoustically open metal grid was located. This array is expected not to affect the spectral broadening on the farfield microphones. The acoustic data were acquired at a sample rate of 102.4 kHz and a measurement time of 50 s. The data were processed using an FFT block size of 65536 and a Hanning window with 50% overlap, yielding 156 averages and a frequency resolution of 1.56 Hz. All data were corrected for wind tunnel background noise and data with a signal-to-noise ratio less than 3 dB were discarded.

Examples of spectral broadening for different microphone positions, source frequencies, and wind speeds are shown in Figure 13 to Figure 15. The legend indicates the calculated propagation angles θ (average of propagation angles inside and outside the flow) and between brackets the estimated values of Δf (to be discussed below). To limit the number of spectra in each figure, only every other microphone is plotted. For the upstream microphone positions the spectra are qualitatively similar to the PLST spectra: a central tone accompanied by two sidelobes. However, for the more downstream microphone positions, where the shear layer becomes thicker, more scattering occurs and the sidelobes are not visible anymore. Similarly to the PLST, the frequency shift Δf decreases with increasing shear layer thickness, as expected on the basis of Eq. (31). For the PLST it was found that $l/\delta_{CA} \approx 4.2$, so that $\Delta f \approx U_0/8.4\delta_{CA}$. Applying this relation to the LLF yields the frequency shifts indicated in the legends of Figure 13 to Figure 15. Since no aerodynamic data were available for the LLF, δ_{CA} was calculated assuming that the LLF has the same spreading parameter $\sigma = 11$ as the PLST. It can be seen that the calculated frequency shifts describe the sidelobe positions reasonably well, suggesting that for the LLF also $l/\delta_{CA} \approx 4.2$ and $\sigma \approx 11$.

Figure 13 to Figure 15 also show that the amount of energy in the sidelobes increases with increasing frequency, wind speed, and shear layer thickness, as expected on the basis of Eq. (29) and confirmed previously for the PLST. For the LLF, the dependence of the energy ratio E_p/E_{tot} on the broadening parameter β was assessed as follows. Since for many cases no clear local minima are present around the main peak, E_p was calculated by simply summing the acoustic energy in the 5 frequency bands centred around the peak. These frequency bands generally included the complete tone (Figure 16). For E_{tot} all energy within ± 1000 Hz of the peak was integrated. The value of β was determined from Eq. (30), assuming the same values of $\sigma = 11$ and $T_v = 0.13$ as in the PLST. Not all measured data could be used for the present assessment: for low frequencies (1 kHz and 2 kHz) the signal-to-noise ratio was too low for some cases, and for frequencies of 16 kHz and higher no peak was visible in the spectra for most microphones (strong scattering).

The results for all usable measurements are shown in Figure 17 and Figure 18. It can be seen that for small values of β (high energy ratio) the experiments follow the theoretical curve reasonably well. However, for larger β the measured energy ratios are higher than the theoretical curve and show substantial scatter. Part of the increased energy ratio and scatter can be explained by the fact that, due to the thick shear layer, the frequency shift Δf becomes very small, so that the energy in the sidelobes contributes to the peak level. To illustrate this, all cases with an estimated Δf (as explained above) smaller than 8 Hz are indicated by circles in Figure 17 and Figure 18. It can be seen that the remaining crosses show much less scatter, although they are still higher than the theoretical curve for large β . It was verified that these increased energy ratios are not due to a limited signal-to-noise ratio (which may limit the usable frequency range for the calculation of E_{tot}).

Another possible explanation for the increased energy ratios in the LLF could be that the assumed values of $\sigma = 11$ and $T_v = 0.13$ (based on the PLST) are not valid for the LLF. For example, decreasing T_v by 10% and increasing σ by 10% will reduce β^2 by a factor of 1.5, bringing the experimental values closer to the theoretical curve. However, there is no physical reason why the values of T_v and σ would be different in the LLF. It should be noted that in the PLST spectra (Figure 6 to Figure 9) the dips beside the main peak were generally more than 10 dB below the peak level. In the LLF (Figure 13 to Figure 15) the level difference is often less than 10 dB due to strong scattering by the thicker shear layer. It could be that the simple theoretical model for spectral broadening breaks down in the case of too strong scattering.

Finally, the increased energy ratios could also be due to the fact that the vortex train assumption, on which the analysis in Section II is based (starting from Eq. (24)), is no longer valid for thick shear layers.

In conclusion, the applicability of the present theoretical model to retrieve original tone levels in the DNW-LLF appears to be limited, for a number of reasons. First, for frequencies of 16 kHz and higher the tone cannot be clearly identified in the spectrum for most microphone positions, because it has become a broad hump. Second, for the cases where a tone *can* be identified, there is no univocal relation between the energy ratio and β , because part of the scattered energy contributes to the peak level if Δf becomes too small. For the limited number of remaining cases where Δf is large enough, there appears to be a more or less univocal relation between the energy ratio and β , so that the original tone level may be retrieved. The reason why the experimental E_p/E_{tot} vs. β^2 curve deviates from theory is not fully clear at present.

4.3 NLR-KAT tunnel

Both aerodynamic and acoustic measurements were carried out in the NLR-KAT tunnel, using the $0.38 \times 0.51 \text{ m}^2$ rectangular nozzle with an extension plate mounted to the vertical 0.51 m side of the nozzle. The test set-up was similar to the PLST set-up shown in Figure 1. All aerodynamic and acoustic measurements were done on the vertical shear layer at $y = 0$. By comparing hotwire results with and without the extension plate, it was verified that the plate had practically no effect on the shear layer at $y = 0$. Using an inflow-microphone, it was verified that spectral broadening by the boundary layer over the extension plate was negligible compared to the broadening by the shear layer. Measurements with an inflow noise source (without nozzle extension plate) yielded similar results as for the set-up with the nozzle extension plate. Therefore, in this subsection only the measurements with nozzle extension plate are discussed. The test hall was treated with foam to suppress acoustic reflections. A speaker (1" BMS compression driver) was installed in the nozzle extension plate, at tunnel axis height and axial distances of 0.27, 0.52, 1.02 and 1.52 m downstream of the nozzle. The speaker produced tonal noise with frequencies between 1 and 48 kHz, and measurements were taken at wind speeds of 50, 60 and 70 m/s. Outside the opposite shear layer an axial row of farfield microphones was placed at tunnel axis height and a lateral distance of 0.69 m to the tunnel axis (0.50 m from the centre of the shear layer). The acoustic data were acquired at a sample rate of 131.072 kHz and a measurement time of 20 s. The data were processed using an FFT block size of 131072 and a Hanning window with 50% overlap, yielding 39 averages and a frequency resolution of 1.0 Hz. All data were corrected for wind tunnel background noise and data with a signal-to-noise ratio less than 3 dB were discarded.

Similarly to the PLST tests, the aerodynamic measurements were done by traversing a cross-wire horizontally through the shear layer, at tunnel axis height and at three axial stations. The normalised mean axial velocity profiles are shown in Figure 19. It can be seen that the shear layer flow is self-similar and matches the Görtler solution from Eq. (9) with $\sigma = 9$, $x_0 = 0$ and $\xi_0 = 0.45$ (compared to $\sigma = 11$ and $\xi_0 = 0.32$ in the PLST), in line with the literature values of Eq. (12). Thus, the KAT shear layer is about 20% thicker than the (untripped) PLST shear layer at the same axial distance. The turbulence intensity profiles at the three axial stations are shown in Figure 20. The maximum turbulence intensities are in line with the literature values mentioned above Eq. (28) and similar to the PLST (Figure 3). However, the scatter turns out to be larger in the KAT than in the PLST. The turbulence spectra in the KAT (not shown) had a broadband character without tonal components, indicating the absence of periodic vortex shedding.

The influence of wind speed, source frequency, source position and microphone position on the spectral broadening in the KAT is shown in Figure 21 to Figure 24. The general trends are similar to the PLST and the LLF:

Δf increases with wind speed and decreases with shear layer thickness, while the energy ratio E_p/E_{tot} decreases with increasing speed, frequency and shear layer thickness. Note that for the highest frequencies in Figure 22 strong scattering occurs, and no sidelobes are present. The value of the length scale l in Eq. (31) was estimated by plotting $U_0/\Delta f$ as a function of x for a large number of measurements with clear sidelobes (source frequencies of 4, 8 and 16 kHz). Using $\sigma = 9$ and Eqs. (18) and (14) to estimate δ_{CA} , this leads to an estimated value of $l/\delta_{CA} \approx 4.0$, which is line with the estimate of 4.2 for the PLST and the values of 3.2 and 4.4 suggested by Candell et al⁷ and McAlpine et al¹⁵, respectively.

The energy ratio E_p/E_{tot} was determined in the same way as for the PLST. E_p was calculated by integrating the acoustic energy between the two local minima around the peak, which were found by smoothing the spectra using a 4-point moving average. For E_{tot} all energy within ± 2000 Hz of the peak was integrated. Based on the aerodynamic results, the value of β was determined from Eq. (30) with $\sigma = 9$ and $T_v = 0.16$ (for $x_s = 0.27$ m and $x_s = 0.52$ m) or $T_v = 0.13$ (for $x_s = 1.02$ m and $x_s = 1.52$ m). The results for the different source positions are shown in Figure 25 to Figure 28. Each figure contains data for wind speeds of 50, 60, and 70 m/s, source frequencies of 2, 4, 8, 16 and 24 kHz, and several microphone positions (normal and oblique passage of the shear layer). The range of propagation angles is indicated in the caption. It can be seen that for each source position the data collapse on a single experimental curve (for $x_s = 1.52$ m the scatter is larger, presumably due to the fact that the shear layer thickness is roughly equal to the width of the test section). This indicates that the normalisation in terms of energy ratio as a function of β^2 effectively collapses different wind speeds and source frequencies on a single curve.

However, in contrast to the PLST, the experimental curve deviates from the theoretical curve, and depends on the axial source position. It can be seen that the energy ratio (as a function of the *normalised* broadening parameter β^2) increases with axial source distance, i.e., with increasing shear layer thickness. This suggests that the increase in spectral broadening with increasing axial source position is slower than expected on the basis of the theory. The fact that the experimental curves for the smaller source axial distances are *below* the theoretical curve, suggests that at these distances the spectral broadening is stronger than expected on the basis of the theory. This cannot be explained by a non-linear growth of the shear layer thickness, since the aerodynamic results indicated that the shear layer is self-similar (Figure 19). Neither can it be explained by a variation in the turbulence intensity T_v , since the measured values were used to calculate β . Thus, it appears that in the KAT certain assumptions of the simplified theory are violated, and affect the results.

For example, it is assumed that the amplitude α in Eq. (1) is not affected by the shear layer, although analysis of the time signals on the microphones shows that substantial amplitude variations occur. Furthermore, above Eq. (5) it is assumed that the function ζ is Gaussian, which is probably not true in reality. For the estimation of the time delay variations in Section II several assumptions and simplifications were made. These assumptions may be checked by determining the actual time delay variations from the experiments (using the time signals from source and microphones), and analysing the frequency content and rms amplitude of $\varepsilon(t)$ as a function of wind speed, source position and source frequency. The measured $\varepsilon(t)$ can also be used to determine the shape function $\Psi(f)$ from Eq. (5), which can be compared to the measured shape functions. Preliminary investigations on the above subjects were carried out, but a conclusive explanation for the deviations between theory and experiment has not been obtained yet.

4.4 DNW-NWB tunnel

For a 4th comparison both acoustic and aerodynamic measurements were carried out in the DNW-NWB low speed wind tunnel. This is a closed-circuit wind tunnel ('Göttingen type') with the possibility to change between open and closed test section. All measurements were conducted in the open test section with a nozzle size of 3.25×2.8 m². The anechoic plenum has a size of $14 \times 16 \times 8$ m³ with an anechoic damping for a frequency range from 250 Hz up to 40 kHz.

The acoustic and aerodynamic measurements were conducted successively in order to minimize the acoustic and hydrodynamic interference. For the aerodynamic measurements a cross hot-wire probe was traversed horizontally through the shear layer $y = 0$ at $x = 1.42$ m, 1.92 m and 2.42 m downstream of the nozzle. The aerodynamic

measurements were conducted at wind speeds of 30 m/s, 60 m/s and 80 m/s. The data were recorded for 10s at a rate of 50 kHz. The normalised mean flow velocities in the shear layer at 30 m/s, 60 m/s and 80 m/s are shown in Figure 29 and Figure 30. The figures show that the shear layers are self-similar and match the Görtler solution with $\sigma = 11$ and $\xi_0 = 0.3$ (comparable to the PLST measurements). The turbulence intensities for the in-flow and horizontal directions are shown in Figure 31. It can be seen that the measurements show only small variations between the three different velocities. The maxima of the turbulence intensity have values of 17% and 12% for the axial and lateral turbulence, respectively. They are comparable to the turbulence maxima measured in the PLST. The lateral turbulence measured at $U_0 = 30$ m/s ($T_v = 0.1161$), $U_0 = 60$ m/s ($T_v = 0.1189$) and $U_0 = 80$ m/s ($T_v = 0.1233$) were linearly interpolated in between these three values.

For the acoustic measurements the loudspeaker was placed 1.92 m downstream of the nozzle. The speaker was placed in the centre of the core flow. The microphone (1/2" LinearX M51) was placed at the same height ($z = 0$) outside of the shear layer at a position of $x = 2.37$ m downstream the nozzle and $y = 3.42$ m from the centre of the core flow. The speaker was driven with tonal noise at frequencies $f_0 = 2$ kHz, 4 kHz, 8 kHz, 16 kHz, 24 kHz and 32 kHz, and at wind speeds of 10, 20, 30, 40, 50, 60, 70 and 80 m/s. The loudspeaker of type ELAC 4PI was covered aerodynamically as described by Kröber et al²². 500s of acoustic data were recorded at a sampling rate of 131.072 kHz for the wind speeds of 30 m/s, 60 m/s, and 80 m/s. Data at the other wind speeds were recorded at the same rate, but only for 60s. Data were processed using an FFT with a block size of 131072 samples, Hanning window, and 50% overlap, which resulted a frequency resolution of 1 Hz. The number of averages was 999 for the 500s-length cases, and 119 for the 60s-measurements. All data were corrected for wind tunnel noise.

In Figure 32 and Figure 33 examples of the influence of wind speed and peak frequency on the spectral broadening are shown. The spectral broadening increases with the peak frequency f_0 while the frequency shift between peak and sidelobe, Δf , remains more or less unaffected. These trends are in accordance to the results at the LLF, KAT and PLST. It can be seen that the peak-to-sidelobe ratio decreases with the peak frequency up to 16 kHz where it remains the same at 24 kHz and even increases at 32 kHz. An example of the effect of wind speed on spectral broadening is shown in Figure 33, where the peak frequency is 16 kHz. The spectral broadening and Δf increase with wind speed and the minima between peak and sidelobe are only visible up to 60 m/s. At 70 m/s and 80 m/s the peak and sidelobes are barely visible indicating strong scattering and are therefore not entered in the subsequent analysis.

Figure 34 shows the experimental results of the energy ratio between the peak energy E_p and the total energy E_{tot} in comparison with the theoretical results of Eq. (29). In accordance with the measurements in the LLF, KAT and PLST, E_p was calculated by integrating the acoustic energy between the two local minima around the peak, using the spectra smoothed with a 4-point moving average. The value of β was determined from Eq. (30) with $\sigma = 11$ and the linear interpolation of the experimental determined lateral turbulence. It can be seen that the energy ratio of the weak scattering coincides well with the curve predicted by Eq. (29).

5 Conclusions

This paper describes a theoretical and experimental study of spectral broadening by shear layers of open jet wind tunnels. The spectral broadening is assumed to be caused by random variations in the propagation time between source and microphone. The time delay variations are due to the turbulence in the shear layer. Applying several assumptions and simplifications, a simple physical model is obtained which predicts the amount of broadening (loss of acoustic energy in a tone) as a function of a few experimental parameters. A broadening parameter β is defined which is proportional to wind speed, source frequency and shear layer thickness.

The theory is tested using experimental data from five different wind tunnels. For the DNW-PLST, the DNW-NWB, and the VKI wind tunnel the agreement between theory and experiment is good. For the complete range of wind speeds, source frequencies and axial source positions, the amount of broadening (i.e., the energy ratio) only depends on the value of the broadening parameter, which can be easily determined for a given test set-up. This

univocal relation between the broadening parameter and the peak energy loss makes it possible to retrieve the original level of a tone from a broadened spectrum, as long as the tone can be identified.

In the DNW-LLF wind tunnel the agreement between experiment and theory is less good. The shear layer is much thicker than in the other tunnels, because the source is positioned more downstream. As a result more broadening occurs, and for frequencies of 16 kHz and higher the tone cannot be clearly identified in the spectrum for most microphone positions. For the cases where a tone *can* be identified, there is no univocal relation between the energy ratio and β . This is because part of the scattered energy contributes to the peak level, due to the small distance between the main peak and the sidelobes, or because the assumptions made in this study are invalid for thick shear layers. Thus, the applicability of the present theoretical model to retrieve original tone levels in the DNW-LLF appears to be limited.

For the NLR-KAT wind tunnel, a univocal relationship is found between β and the energy ratio for the complete range of wind speeds and source frequencies. This offers the possibility to retrieve the original tone level from the broadened spectrum. However, the relationship between β and energy ratio is found to depend on the source position, which limits the applicability of the theory for this tunnel. The discrepancy between theory and experiment is probably caused by some violation of the theoretical assumptions and simplifications.

The present work can be extended in several ways. First, to check the theoretical assumptions and simplifications, the present experimental database can be analysed in more detail, as discussed at the end of Section IV.C. Such an analysis could include for example amplitude fluctuations and the amplitude and spectral content of the time delay variations. Furthermore, it would be interesting to investigate the nature and characteristics of the asymmetry in the broadened spectra for oblique propagation angles, and the dependence of the wind speed and shear layer thickness on sidelobe frequency shift.

As explained in the Introduction, one of the objectives of the present investigation was to investigate the possibility to retrieve the original energy of a tone in a broadened spectrum using simple scaling rules. The theoretical model that was developed in this study proved to be very useful for that purpose. However, this study also shows that the applicability of this correction method has its limits. Therefore, it is recommended to investigate also alternative methods to reduce the effects of spectral broadening. These may include for example more advanced prediction methods, application of the 'Guide Star' method^{24,25} to correct for time delay variations, the use of 'aerodynamically closed and acoustically open' tunnel walls²⁶ to replace the thick shear layer by a thin boundary layer, or development of improved inflow microphone measurements.

Appendix A The relation between spectral broadening and time delay variations

A theory is discussed about the relation between spectral broadening and time delay variations between source and microphone. The time delay variations can be due to turbulence in a wind tunnel shear layer, through which sound is travelling that is generated inside the wind tunnel jet. The theory is presented here to provide some insight in the mechanism of spectral broadening. More thorough theoretical approaches can be found in the literature¹⁰⁻¹⁵.

A.1 Some definitions

Fourier transform

The Fourier transform $P = \mathfrak{F}(p)$ of a time series $p(t)$ is defined by

$$P(f) = \int_{-\infty}^{\infty} e^{-2\pi ift} p(t) dt . \quad (35)$$

The inverse Fourier transform is

$$p(t) = \int_{-\infty}^{\infty} e^{+2\pi ift} P(f) df . \quad (36)$$

Generalised functions

We will consider generalised functions here²⁷. A well-known example is the Dirac-delta function $\delta(x)$. This is an “infinitely sharp peak” at $x = 0$. It is zero for $x \neq 0$, and the integrated value is 1. More generally, if $a(x)$ is a smooth function, then

$$\int_{-\infty}^{\infty} \delta(x - y) a(y) dy = a(x) . \quad (37)$$

For generalised functions Fourier transforms can be defined in a generalised sense. A typical example is the Fourier transform of $p(t) = 1$:

$$P(f) = \int_{-\infty}^{\infty} e^{-2\pi ift} dt = \delta(f) . \quad (38)$$

Convolution

The convolution between two functions $a(x)$ and $b(x)$ is defined by

$$a(x) * b(x) = \int_{-\infty}^{\infty} a(x - y) b(y) dy . \quad (39)$$

Convolution can also be defined for generalised functions (under certain conditions). For the Fourier transform \mathfrak{F} , we have

$$\mathfrak{F}(a * b) = \mathfrak{F}(a) \mathfrak{F}(b) . \quad (40)$$

Convolution with a Dirac-delta function yields

$$\delta(x - y) * a(x) = a(x - y) . \quad (41)$$

Cross-correlation and cross-spectrum

Assuming that $p(t)$ and $q(t)$ are locally square-integrable time series, we can define their cross-correlation function by

$$R_{pq}(t) = \lim_{T \rightarrow \infty} \frac{1}{2T} \int_{-T}^T p(\tau)^\dagger q(t + \tau) d\tau , \quad (42)$$

where \dagger denotes complex conjugation. This can also be written as an expectation value

$$R_{pq}(t) = E\{p(\cdot)^\dagger q(t + \cdot)\}. \quad (43)$$

The cross-spectrum $A_{pq}(f)$ is the Fourier transform of $R_{pq}(t)$. This can be written as

$$A_{pq}(f) = \int_{-\infty}^{\infty} e^{-2\pi ift} R_{pq}(t) dt = \lim_{T \rightarrow \infty} \frac{1}{2T} \left(\int_{-T}^T e^{-2\pi ift} p(t) dt \right)^\dagger \left(\int_{-T}^T e^{-2\pi ift} q(t) dt \right). \quad (44)$$

We have:

$$\int_{-\infty}^{\infty} e^{2\pi ift} A_{pq}(f) df = R_{pq}(t), \quad (45)$$

and, consequently, for $p = q$,

$$\int_{-\infty}^{\infty} A_{pp}(f) df = R_{pp}(0) = \lim_{T \rightarrow \infty} \frac{1}{2T} \int_{-T}^T |p(\tau)|^2 d\tau = E\{|p(\cdot)|^2\} = p_{\text{rms}}^2. \quad (46)$$

In other words, there is conservation of acoustic energy.

A.2 General expressions

Suppose that a single-frequency sound source is placed inside a jet, and its sound is received by microphones outside the jet. Then the measured signal is transmitted through the turbulent shear layer, which causes distortions in phase and amplitude²⁵. If the emitted sound has frequency f_0 , then a microphone receives the signal:

$$p(t) = \alpha(t) \exp(2\pi if_0(t + \Delta t + \varepsilon(t))) \quad (47)$$

where Δt is the average time delay, $\varepsilon(t)$ the time delay variation, and $\alpha(t)$ the time-dependent (real-valued) amplitude. In the following, we ignore¹ the time-dependency of $\alpha(t)$, so that we simply have

$$p(t) = \alpha \exp(2\pi if_0(t + \Delta t + \varepsilon(t))). \quad (48)$$

The auto-correlation function $R_{pp}(t)$ of $p(t)$ is given by

$$R_{pp}(t) = E\{p(\cdot)^\dagger p(t + \cdot)\} = \alpha^2 \exp(2\pi if_0 t) \psi(t), \quad (49)$$

with

$$\psi(t) = E\{\exp(2\pi if_0(\varepsilon(t + \cdot) - \varepsilon(\cdot)))\}. \quad (50)$$

The auto-spectrum $A_{pp}(f)$ follows by taking the Fourier transform of (49):

$$A_{pp}(f) = \mathfrak{F}[R_{pp}(t)](f) = \alpha^2 \mathfrak{F}[\exp(2\pi if_0 t) \psi(t)] = \alpha^2 \Psi(f - f_0), \quad (51)$$

where $\Psi(f)$ is the Fourier transforms of $\psi(t)$. Looking at the acoustic energy, we have

$$p_{\text{rms}}^2 = \int_{-\infty}^{\infty} A_{pp}(f) df = \alpha^2 \int_{-\infty}^{\infty} \Psi(f - f_0) df = \alpha^2, \quad (52)$$

where we used the fact that

$$\int_{-\infty}^{\infty} \Psi(f) df = \psi(0) = 1. \quad (53)$$

In the following, $\Psi(f)$ is referred to as the ‘‘shape function’’, because it describes the shape of the measured spectrum.

¹ This simplification is very convenient, but possibly too crude.

A.3 Evaluation of shape function

In the previous subsection, it was derived that $\psi(t)$, Eq. (50), and its Fourier transform $\Psi(f)$ determine the shape of the spectrum $A_{pp}(f)$. We can write

$$\psi(t) = E \{ g(\cdot)^\dagger g(t+\cdot) \} = R_{gg}(t), \quad (54)$$

with

$$g(t) = \exp(2\pi i f_0 \varepsilon(t)). \quad (55)$$

Consequently,

$$\Psi(f) = A_{gg}(f). \quad (56)$$

It is noted that the shape function $\Psi(f)$ does not need to be symmetric around $f = 0$, since $g(t)$ is not real-valued. In the following, two approximations are discussed for which $\Psi(f)$ is symmetric nevertheless:

- (a) the time delay variation is small compared to the period of the driving frequency f_0 ,
- (b) the (random) process $\tau \rightarrow \varepsilon(t+\tau) - \varepsilon(\tau)$ is Gaussian for all values of t .

These two cases are discussed in the following.

For convenience, we define

$$\zeta_t(\tau) = \varepsilon(t+\tau) - \varepsilon(\tau), \quad (57)$$

so that

$$\psi(t) = E \{ \exp[2\pi i f_0 \zeta_t(t)] \}. \quad (58)$$

Approximation of shape function for small time delay variations

We can expand $\psi(t)$ into a Taylor series:

$$\psi(t) = 1 - \frac{(2\pi f_0)^2}{2!} E \{ \zeta_t^2 \} + \frac{(2\pi f_0)^4}{4!} E \{ \zeta_t^4 \} - \dots \quad (59)$$

Herein, we have:

$$E \{ \zeta_t^2 \} = E \{ (\varepsilon(t+\tau) - \varepsilon(\tau))^2 \} = 2(R_{\varepsilon\varepsilon}(0) - R_{\varepsilon\varepsilon}(t)) = 2(\varepsilon_{\text{rms}}^2 - R_{\varepsilon\varepsilon}(t)), \quad (60)$$

where $R_{\varepsilon\varepsilon}(t)$ is the auto-correlation function of $\varepsilon(t)$. Thus, the first order approximation is

$$\psi(t) \approx 1 - (2\pi f_0)^2 (\varepsilon_{\text{rms}}^2 - R_{\varepsilon\varepsilon}(t)). \quad (61)$$

This should be a good approximation up to $f_0 \varepsilon_{\text{rms}} \leq 0.1$. For the Fourier transform of (61), we have

$$\Psi(f) \approx \left(1 - (2\pi f_0 \varepsilon_{\text{rms}})^2\right) \delta(f) + (2\pi f_0)^2 A_{\varepsilon\varepsilon}(f), \quad (62)$$

in which $A_{\varepsilon\varepsilon}(f)$ is the auto-spectrum of $\varepsilon(t)$.

In Eq. (62) we recognise that the shape function consists of a sharp peak corresponding to the Dirac-delta function, and a broadband spectrum corresponding to the time delay variation $\varepsilon(t)$. As f_0 and/or ε_{rms} increase, the peak contribution decreases and the broadband contribution increases.

The broadband contribution usually appears as a ‘‘hump’’ or as side bands, of which the shapes depend on the characteristics of $\varepsilon(t)$. It is noted that the spectral shape of the broadband contribution is independent of the frequency f_0 . In other words, when the frequency increases the hump does not become wider. Moreover, since the average value of $\varepsilon(t)$ is zero, we see that

$$A_{\varepsilon\varepsilon}(0) = \int_{-\infty}^{\infty} R_{\varepsilon\varepsilon}(t) dt = \int_{-\infty}^{\infty} E \{ \varepsilon(\cdot) \varepsilon(t+\cdot) \} dt = 0. \quad (63)$$

This explains the characteristic ‘‘dip’’ in the side bands, as reported by Candel et al⁶.

The total acoustic energy remains constant:

$$\int_{-\infty}^{\infty} \Psi(f) df \approx \left(1 - (2\pi f_0)^2 \varepsilon_{\text{rms}}^2\right) + (2\pi f_0)^2 \varepsilon_{\text{rms}}^2 = 1, \quad (64)$$

as in the general case, Eq. (53).

Approximation of shape function using Gaussian process assumption

Alternatively, $\Psi(f)$ can be evaluated under the assumption that $\zeta_t(\tau) = \varepsilon(t + \tau) - \varepsilon(\tau)$ is a Gaussian process for any value of t . There is no particular reason why $\zeta_t(\tau)$ should be Gaussian, especially for small values of t , when there is significant coherence between $\varepsilon(t + \tau)$ and $\varepsilon(\tau)$. Nonetheless, it may be expected that the analysis given here predicts some trends which are also valid when $\zeta_t(\tau)$ is non-Gaussian.

When $\zeta_t(\tau)$ is a Gaussian process, its probability density function $D_t(\varphi)$ is given by

$$D_t(\varphi) = \frac{1}{\sigma_t \sqrt{2\pi}} \exp\left(-\varphi^2 / 2\sigma_t^2\right), \quad (65)$$

in which (see also Eq. (60))

$$\sigma_t^2 = E\{\zeta_t^2\} = 2(\varepsilon_{\text{rms}}^2 - R_{\varepsilon\varepsilon}(t)). \quad (66)$$

With (65), Eq. (58) can be evaluated as

$$\begin{aligned} \psi(t) &= \int_{-\infty}^{\infty} D_t(\varphi) \exp(2\pi i f_0 \varphi) d\varphi = \frac{1}{\sigma_t \sqrt{2\pi}} \int_{-\infty}^{\infty} \exp\left(2\pi i f_0 \varphi - \frac{\varphi^2}{2\sigma_t^2}\right) d\varphi = \exp\left(-2\pi^2 f_0^2 \sigma_t^2\right) \\ &= \exp\left(-(2\pi f_0)^2 (\varepsilon_{\text{rms}}^2 - R_{\varepsilon\varepsilon}(t))\right). \end{aligned} \quad (67)$$

Note that for small values of $f_0 \varepsilon_{\text{rms}}$, this approximation is the same as Eq. (61). Assuming that $R_{\varepsilon\varepsilon}(t)$ tends to zero for large values of t , we can write

$$\psi(t) = \exp\left(-(2\pi f_0)^2 (\varepsilon_{\text{rms}}^2 - R_{\varepsilon\varepsilon}(t))\right) = \exp\left(-(2\pi f_0 \varepsilon_{\text{rms}})^2\right) + b(t), \quad (68)$$

with

$$b(t) = \exp\left(-(2\pi f_0 \varepsilon_{\text{rms}})^2\right) \left(\exp\left((2\pi f_0)^2 R_{\varepsilon\varepsilon}(t)\right) - 1\right). \quad (69)$$

The Fourier transform of (68) is

$$\Psi(f) = \exp\left(-(2\pi f_0 \varepsilon_{\text{rms}})^2\right) \delta(f) + B(f), \quad (70)$$

where $B(f)$ is the Fourier transform of $b(t)$.

Again we see that the shape function $\Psi(f)$ consists of a sharp peak (the Dirac-delta function) and a broadband contribution. Since $b(t)$ tends to zero for large values of t , $B(f)$ does not contain a sharp peak. The peak contribution in (70) decays with f_0 and ε_{rms} : more than 20 dB of the peak is lost when $f_0 \varepsilon_{\text{rms}} > 0.34$.

For $f_0 \varepsilon_{\text{rms}} > 0.34$, $\psi(t)$ tends to approximately zero for large t . We also have $\psi(0) = 1$, which means that there is always a region around $t = 0$ for which $\psi(t) \neq 0$. In other words, ψ always has a non-zero support $S(\psi)$:

$$S(\psi) = \{t \in \mathbb{R}; \psi(t) \neq 0\}. \quad (71)$$

For small t , we can write:

$$\psi(t) = E\left\{\exp[2\pi i f_0 t \varepsilon'(\tau)]\right\}. \quad (72)$$

With this, we may expect that the width of the support of $\psi(t)$ is inversely proportional to f_0 . Consequently, the hump of $\Psi(f)$ is expected to become proportionally wider with f_0 .

A.4 Summary

The theory described in this appendix can be summarised as follows. If a pure tone at $f = f_0$ is generated inside a wind tunnel jet, then the auto-spectrum measured by a microphone outside the jet can be approximated by

$$A_{pp}(f) = p_{\text{rms}}^2 \Psi(f - f_0). \quad (51),(52)$$

Herein, Ψ is a shape function, for which

$$\int_{-\infty}^{\infty} \Psi(f) df = 1. \quad (53)$$

Under the assumption that $\zeta_t(\tau) = \varepsilon(t + \tau) - \varepsilon(\tau)$ is a Gaussian process for any value of t , we can write

$$\Psi(f) = \exp\left(-\left(2\pi f_0 \varepsilon_{\text{rms}}\right)^2\right) \delta(f) + B(f), \quad (73)$$

which is built up by a sharp peak (first term) and a broadband hump $B(f)$. The peak contribution diminishes for large values of f_0 and ε_{rms} : more than 20 dB of the peak is lost when $f_0 \varepsilon_{\text{rms}} > 0.34$. For large values of f_0 it is expected that the width (support) of $B(f)$ increases proportionally with f_0 .

For small values of $f_0 \varepsilon_{\text{rms}}$, say for $f_0 \varepsilon_{\text{rms}} < 0.1$, $\Psi(f)$ can be approximated by

$$\Psi(f) \approx \left(1 - (2\pi f_0)^2 \varepsilon_{\text{rms}}^2\right) \delta(f) + (2\pi f_0)^2 A_{\varepsilon\varepsilon}(f), \quad (62)$$

which is also valid when $\zeta_t(\tau)$ is non-Gaussian. The shape of the hump has become independent of f_0 . Since $A_{\varepsilon\varepsilon}(0) = 0$, the hump consists of two sidelobes.

Acknowledgements

This research was carried out within GARTEUR AD/AG-50 “Effect of Open Jet Shear Layers on Aeroacoustic Wind Tunnel Measurements”. Part of the work was sponsored through the DNW Research Support Programme. The authors are grateful to Zana Sulaiman for analysing the KAT data.

References

- ¹ Amiet, R.K., “Correction of Open Jet Wind Tunnel Measurements for Shear Layer Refraction”, AIAA Paper 75-532, 1975.
- ² Amiet, R.K., “Refraction of Sound by a Shear Layer”, AIAA Paper 77-54, 1977.
- ³ Schlinker, R.H., and Amiet, R.K., “Refraction of Sound by a Shear Layer – Experimental Assessment”, AIAA Paper 79-628, 1979.
- ⁴ Ahuja, K.K., Tanna, H.K., and Tester, B.J., “An Experimental Study of Transmission, Reflection and Scattering of Sound in a Free Jet Flight Simulation Facility and Comparison with Theory”, *Journal of Sound and Vibration* Vol. 75, Nr. 1, 1981, pp. 51-85.
- ⁵ Bahr, C., Zawodny, N.S., Yardibi, T., Liu, F., Wetzels, D., Bertolucci, B., and Cattafesta, L., “Shear Layer Time-Delay Correction Using a Non-Intrusive Acoustic Point Source”, *International Journal of Aeroacoustics*, Vol. 10, Nrs. 5&6, 2011, pp. 497-530.
- ⁶ Candel, S., Guedel, A., and Julienne, A., “Refraction and Scattering of Sound in an Open Wind Tunnel Flow”, *Proceedings of the Sixth International Congress on Instrumentation in Aerospace Simulation Facilities*, 1975, pp. 288–300.
- ⁷ Candel, S., Guedel, A., and Julienne, A., “Refraction and Scattering of Acoustic Waves in a Free Shear Flow”, AIAA Paper 76-544, 1976.
- ⁸ Guedel, A., “Scattering of an Acoustic Field by a Free Jet Shear Layer”, AIAA Paper 83-698, 1983.
- ⁹ Guedel, A., “Scattering of an Acoustic Field by a Free Jet Shear Layer”, *Journal of Sound and Vibration*, Vol. 100, Nr. 2, 1985, pp. 285–304.
- ¹⁰ Campos, L.M.B.C., “The Spectral Broadening of Sound by Turbulent Shear Layers; Part 1: The Transmission of Sound Through Turbulent Shear Layers”, *Journal of Fluid Mechanics*, Vol. 89, Nr. 4, 1978, pp. 723-749.
- ¹¹ Campos, L.M.B.C., “The Spectral Broadening of Sound by Turbulent Shear Layers; Part 2: The Spectral Broadening of Sound and Aircraft Noise”, *Journal of Fluid Mechanics*, Vol. 89, Nr. 4, 1978, pp. 751-783.
- ¹² Cargill, A.M., “Sound Propagation through Fluctuating Flows – Its Significance in Aeroacoustics”, AIAA Paper 83-697, 1983.
- ¹³ Ewert, R., Kornow, O., Tester, B.J., Powles, C.J., Delfs, J.W., and Rose, M., “Spectral Broadening of Jet Engine Turbine Tones”, AIAA Paper 2008-2940, 2008.
- ¹⁴ Ewert, R., Kornow, O., Yin, J., Delfs, J.W., Röber, T., and Rose, M., “A CAA Based Approach to Tone Haystacking”, AIAA Paper 2009-3217, 2009.
- ¹⁵ McAlpine, A., Powles, C.J., and Tester, B.J., “A Weak Scattering Model for Tone Haystacking”, AIAA Paper 2009-3216, 2009.
- ¹⁶ Powles, C.J., Tester, B.J., and McAlpine, A., “A Weak Scattering Model for Turbine-Tone Haystacking Outside the Cone of Silence”, *International Journal of Aeroacoustics*, Vol. 10, Nr. 1, 2011, pp. 17-50.
- ¹⁷ Kröber, S., Hellmold, M., and Koop, L., “Experimental Investigation of Spectral Broadening of Sound Waves by Wind Tunnel Shear Layers”, AIAA Paper 2013-2255, 2013.
- ¹⁸ Görtler, H., “Berechnungen von Aufgaben der Freien Turbulenz auf Grund eines Neuen Näherungsansatzes”, *Zeitschrift für Angewandte Mathematik und Mechanik*, Vol. 22, Nr. 5, 1942, pp. 244-254.
- ¹⁹ Abramovich, G.N., *The Theory of Turbulent Jets*, MIT Press, Massachusetts, 1963.
- ²⁰ Wygnanski, I., and Fiedler, H.E., “The Two-Dimensional Mixing Region”, *Journal of Fluid Mechanics*, Vol. 41, Nr. 2, 1969, pp. 327-361.
- ²¹ Liepmann, H.W., and Laufer, J., “Investigations of Free Turbulent Mixing”, NACA Technical Note 1257, 1947.

- ²² Kröber, S., Ehrenfried, K., and Koop, L., “Design and Testing of Sound Sources for Phased Microphone Array Calibration”, BeBeC-2008-02, Berlin Beamforming Conference 2008.
- ²³ Ng, E.W., and Geller, M., “A Table of Integrals of the Error Functions”, *Journal of Research of the National Bureau of Standards - B. Mathematical Sciences*, Vol. 73B, No. 1, 1969.
- ²⁴ Sijtsma, P., “Acoustic Array Corrections for Coherence Loss Due to the Wind Tunnel Shear Layer”, BeBeC-2008-15, Berlin Beamforming Conference 2008.
- ²⁵ Koop, L., Ehrenfried, K., and Kröber, S., “Investigation of the Systematic Phase Mismatch in Microphone-Array Analysis”, AIAA-Paper 2005-2962, 2005.
- ²⁶ Devenport, W., Burdisso, R., Borgoltz, A., Ravetta, P., and Barone, M., “Aerodynamic and Acoustic Corrections for a Kevlar-Walled Anechoic Wind Tunnel”, AIAA Paper 2010-3749, 2010.
- ²⁷ Lighthill, M.J., *Introduction to Fourier Analysis and Generalised Functions*, Cambridge University Press, 1978.

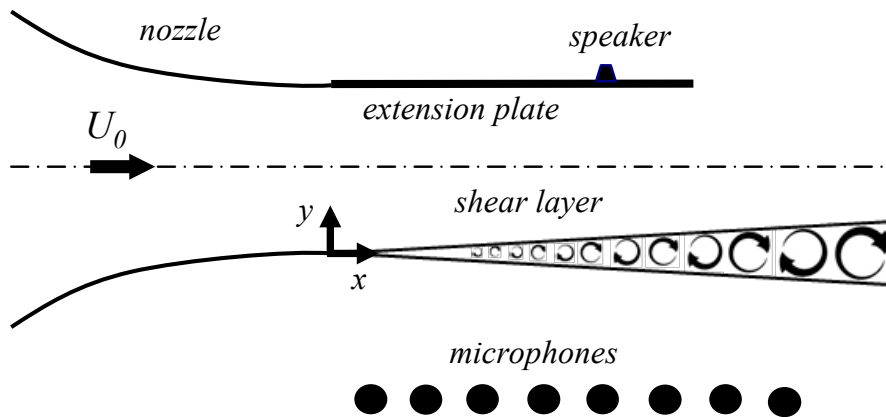


Figure 1: Top view of test set-up for acoustic measurements in DNW-PLST.

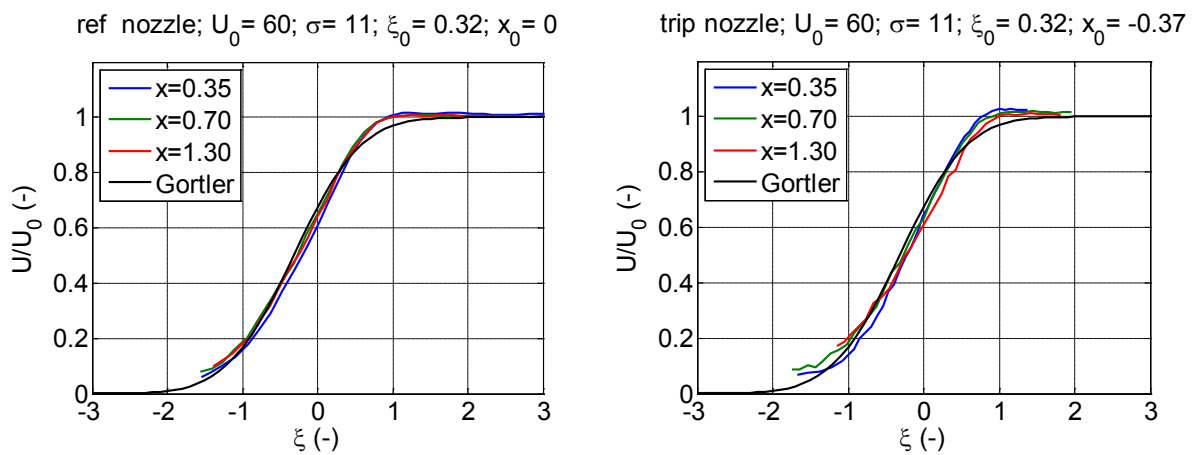


Figure 2: Normalised mean axial velocity profiles at 60 m/s for reference nozzle (left) and tripped nozzle (right). The black line shows the Görtler solution from Eq. (9) with $\sigma=11$.

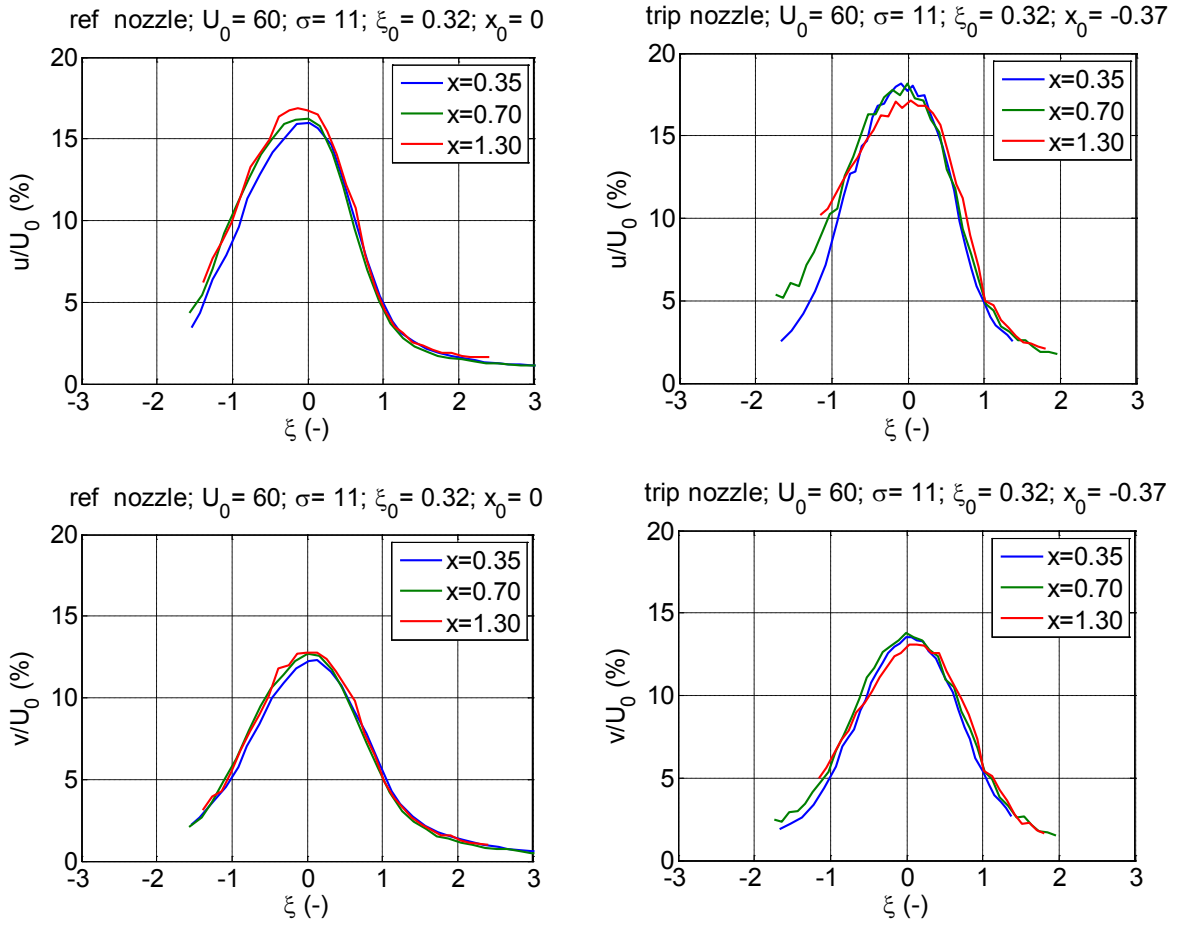


Figure 3: Axial (upper row) and lateral (lower row) turbulence intensity profiles at 60 m/s for reference nozzle (left column) and tripped nozzle (right column).

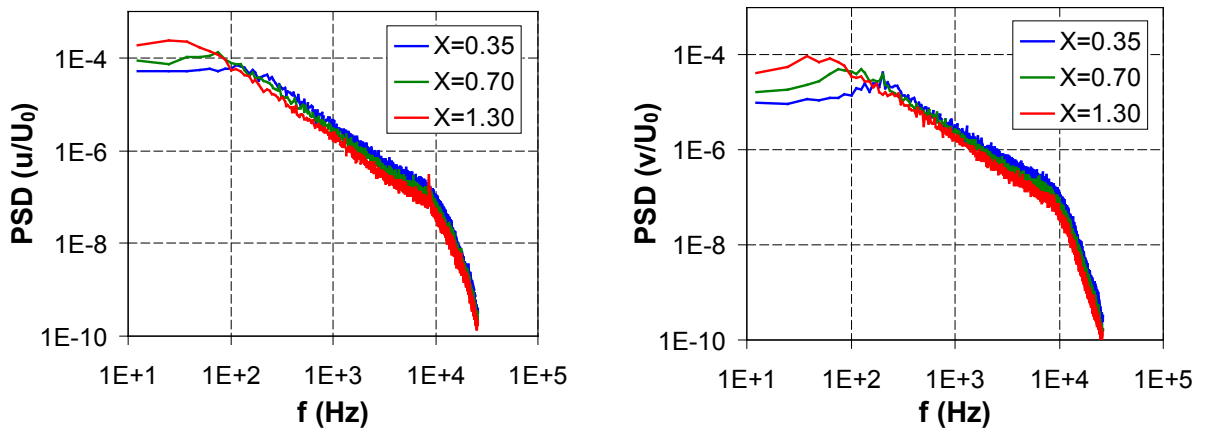


Figure 4: Spectra of axial (left) and lateral (right) turbulence at the centre of the shear layer, for the reference nozzle at 60 m/s.

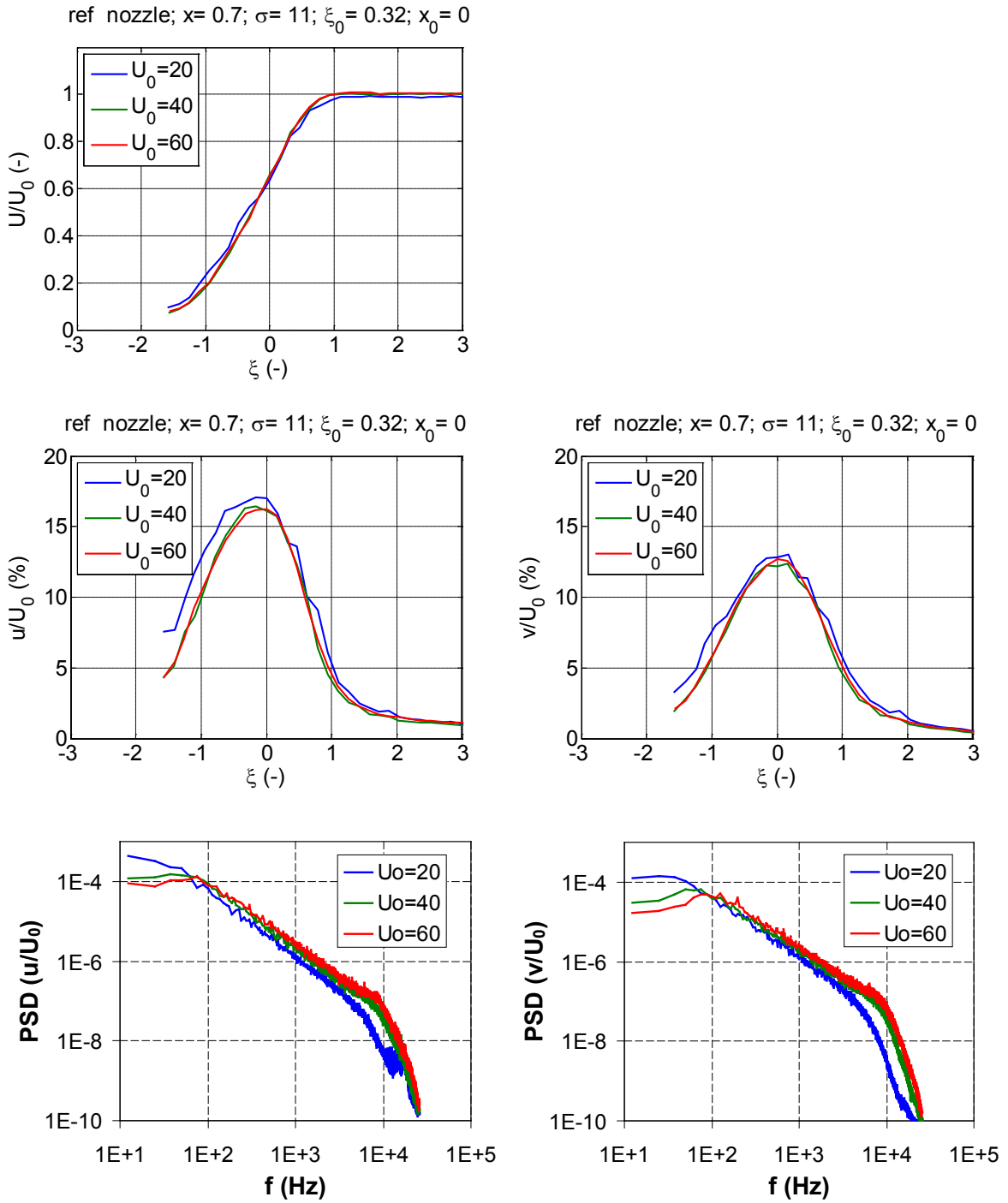


Figure 5: Effect of wind speed on flow properties for reference nozzle at $x=0.7$ m.

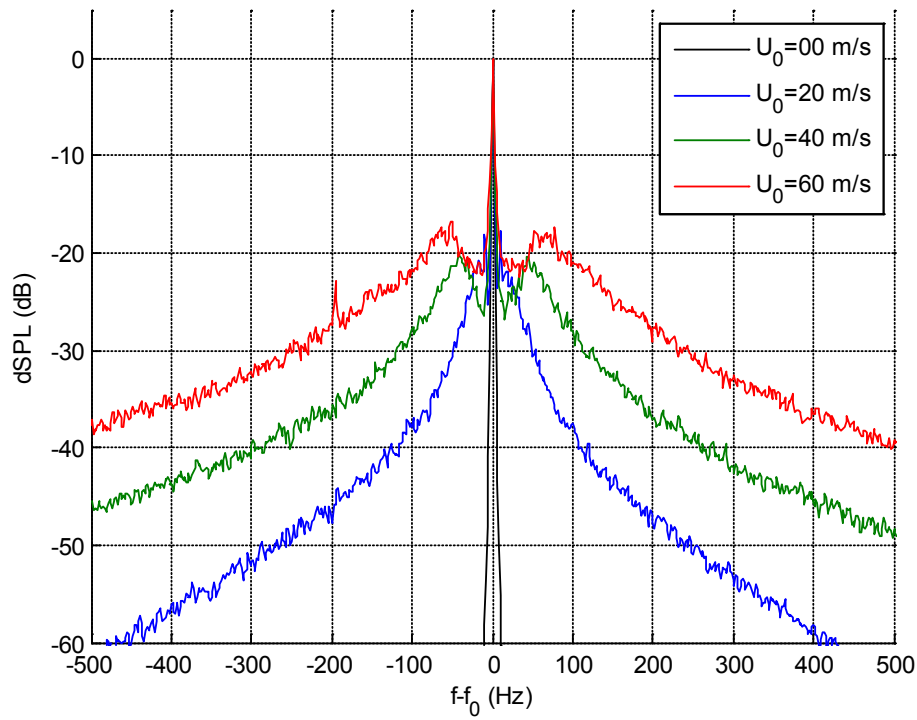


Figure 6: Effect of wind speed on spectral broadening for $x_s=x_m=0.7$ m and $f_0=16$ kHz.

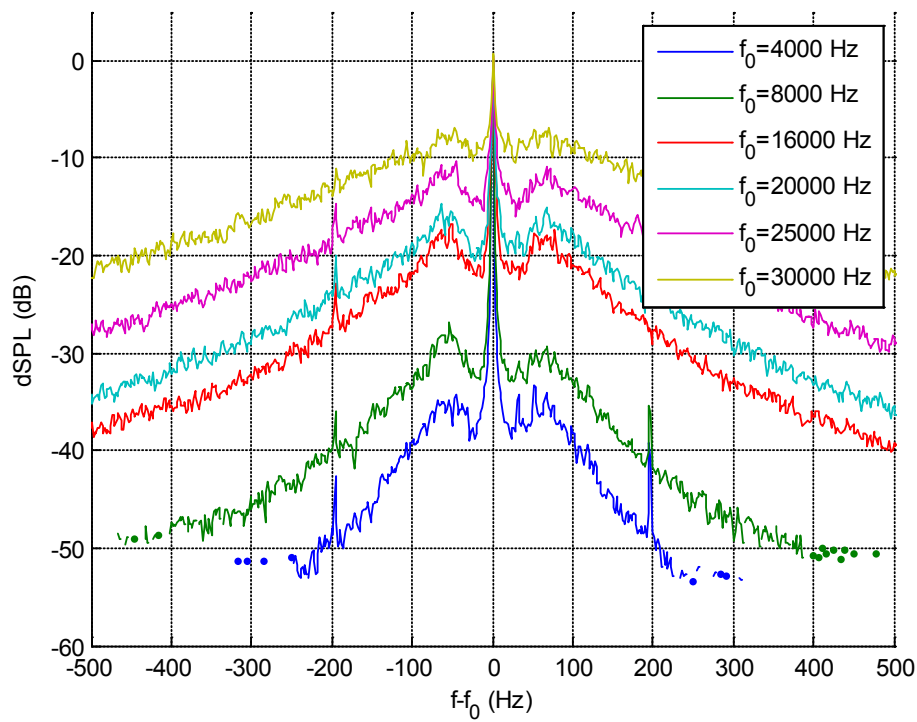


Figure 7: Effect of source frequency on spectral broadening for $x_s=x_m=0.7$ m and $U_0=60$ m/s.

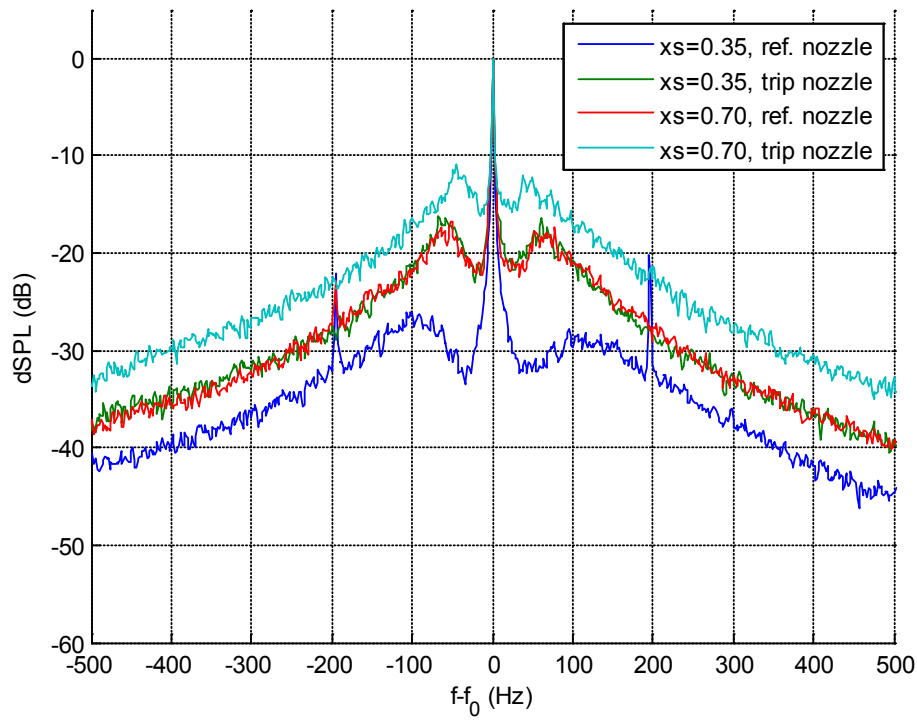


Figure 8: Effect of shear layer thickness on spectral broadening for $f_0=16$ kHz, $x_m=x_s$ and $U_0=60$ m/s.

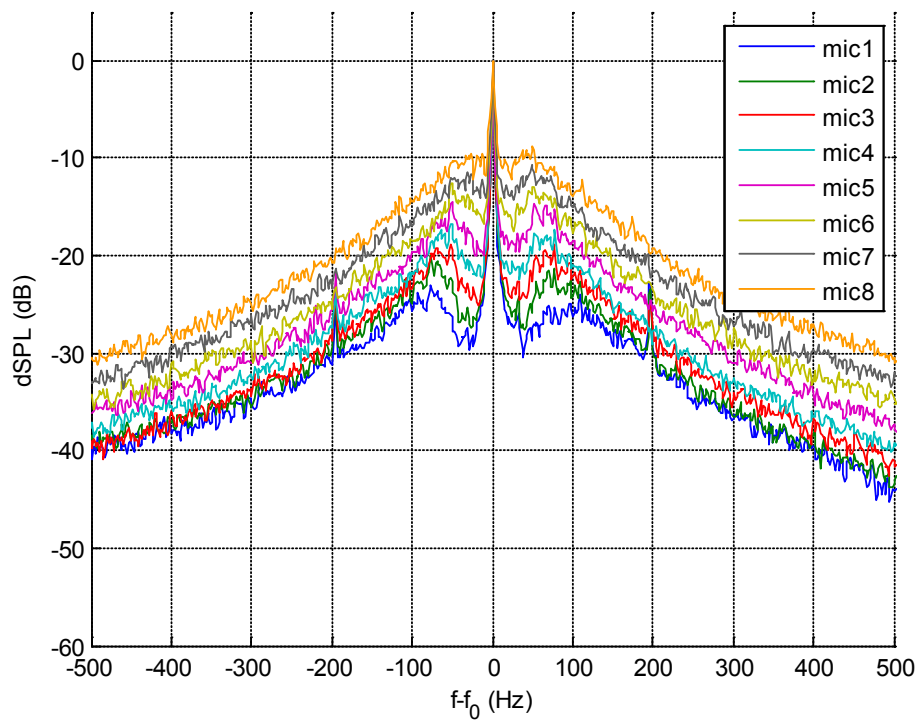


Figure 9: Effect of microphone position on spectral broadening for $x_s=0.7$ m, $f_0=16$ kHz and $U_0=60$ m/s. The microphone number increases with axial position.

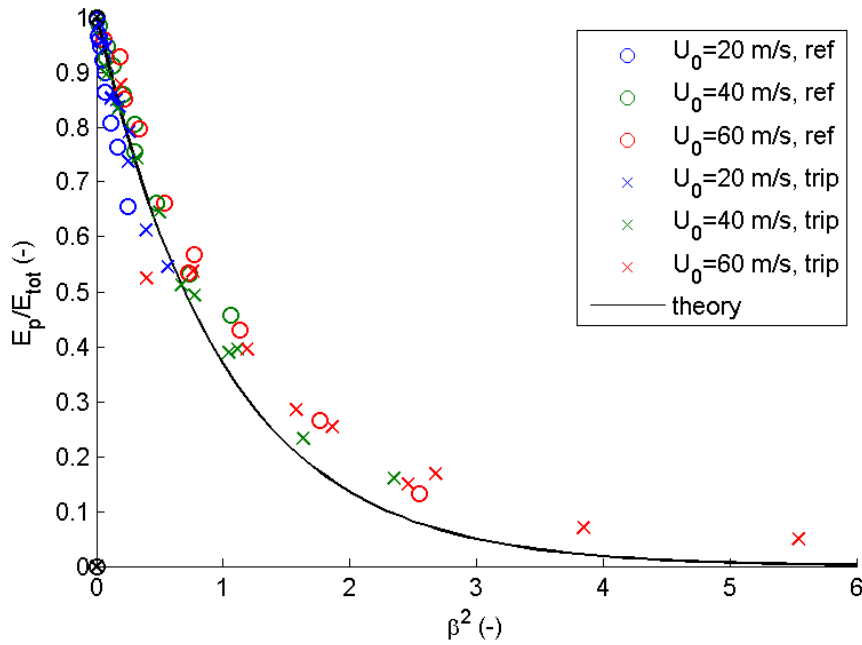


Figure 10: Energy ratio for all measurements with $x_m=x_s$ (normal passage of shear layer). Each series contains data for 5 source frequencies and 2 source positions. The black line shows the theoretical curve from Eq. (29).

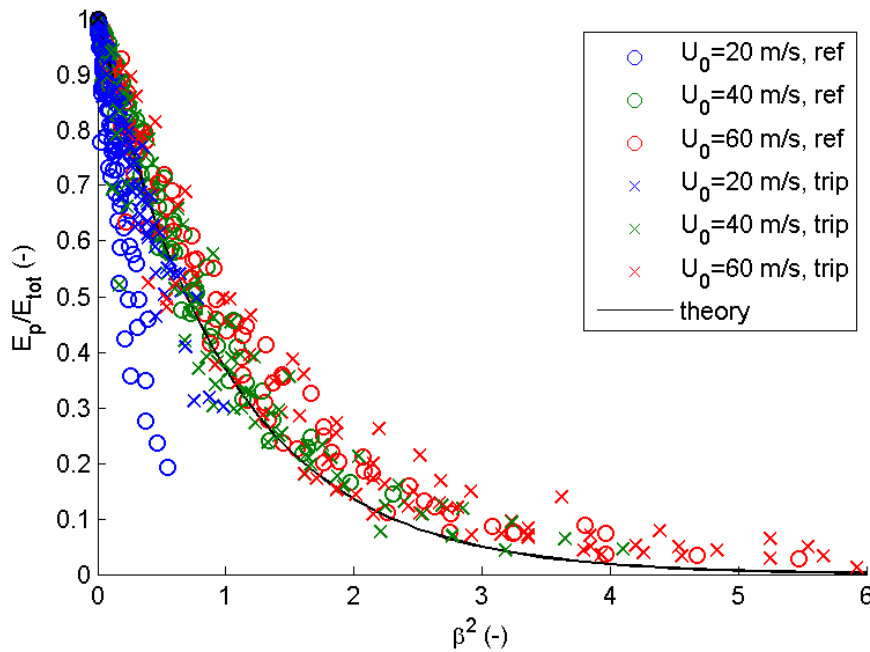


Figure 11: Energy ratio for all measurements including $x_m \neq x_s$ (oblique passage of shear layer). Each series contains data for 5 source frequencies, 2 source positions and 8 microphones. The black line shows the theoretical curve from Eq. (29).

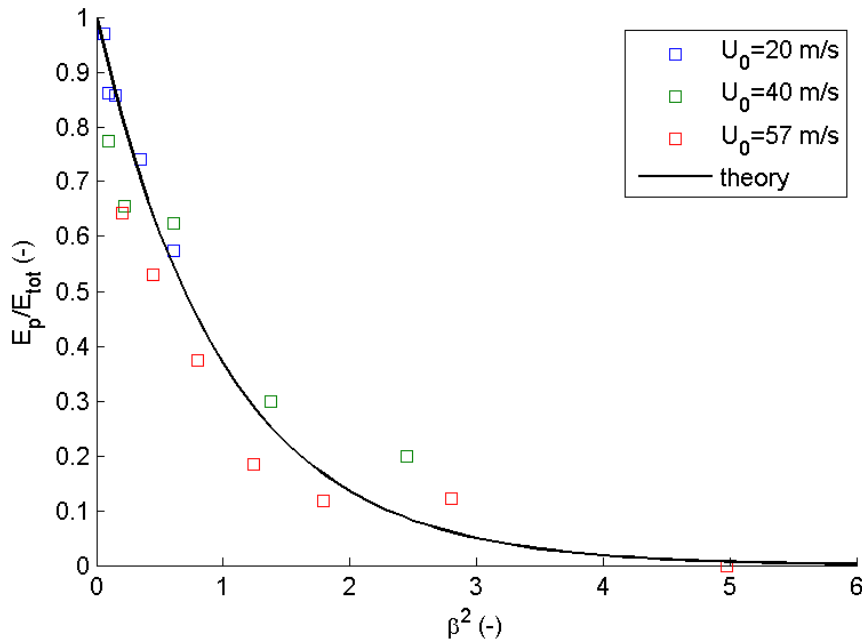


Figure 12: Energy ratio for spectral broadening measurements in VKI tunnel⁶⁻⁹ with $x_m=x_s=1.95$ m (normal passage of shear layer). Each series contains data for different source frequencies. The black line shows the theoretical curve from Eq. (29).

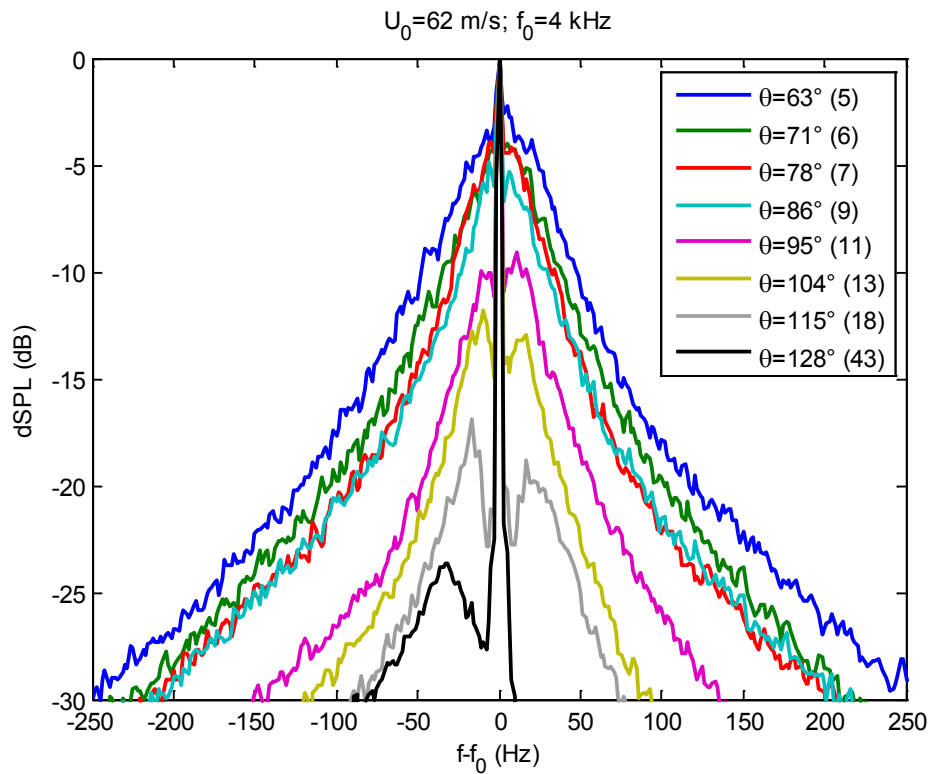


Figure 13: Spectral broadening on an axial row of microphones in the DNW-LLF, for $f_0=4$ kHz and $U_0=62$ m/s. The legend indicates the propagation angle θ and the estimated Δf .

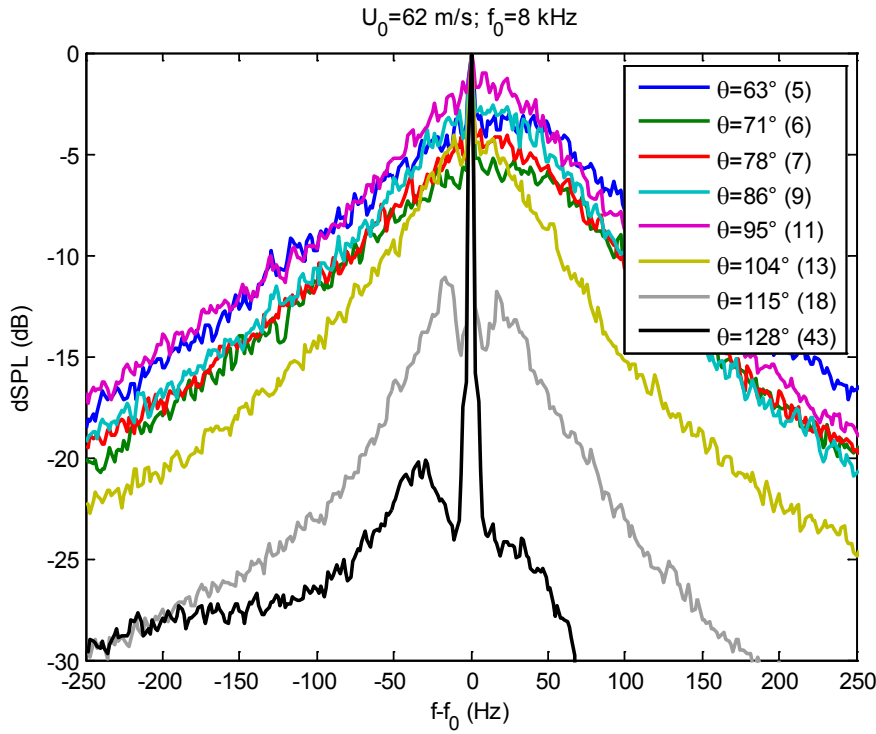


Figure 14: Spectral broadening on an axial row of microphones in the DNW-LLF, for $f_0=8 \text{ kHz}$ and $U_0=62 \text{ m/s}$. The legend indicates the propagation angle θ and the estimated Δf .

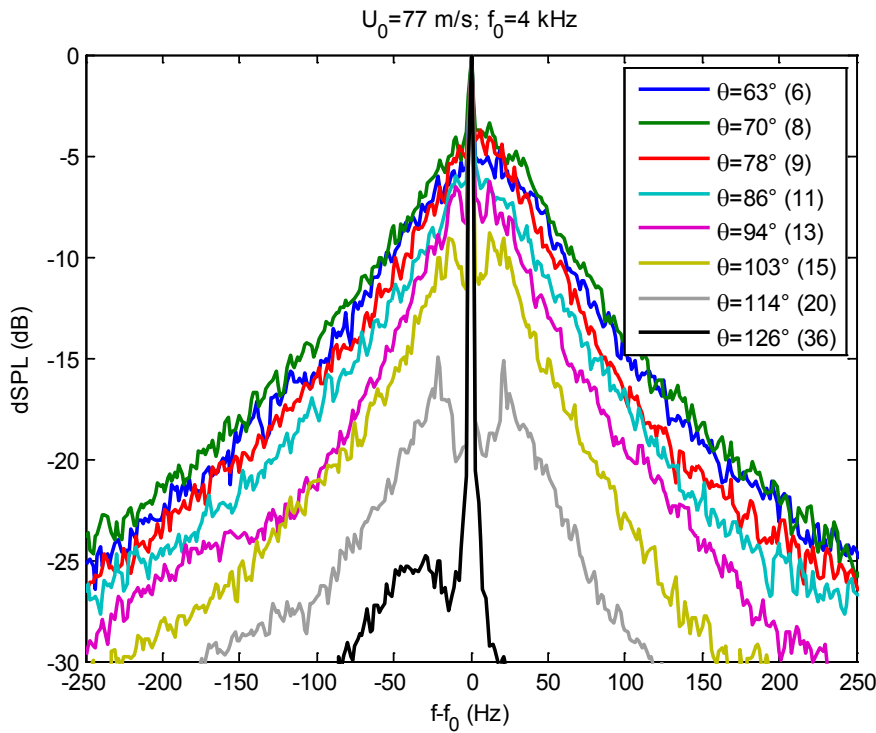


Figure 15: Spectral broadening on an axial row of microphones in the DNW-LLF, for $f_0=4 \text{ kHz}$ and $U_0=77 \text{ m/s}$. The legend indicates the propagation angle θ and the estimated Δf .

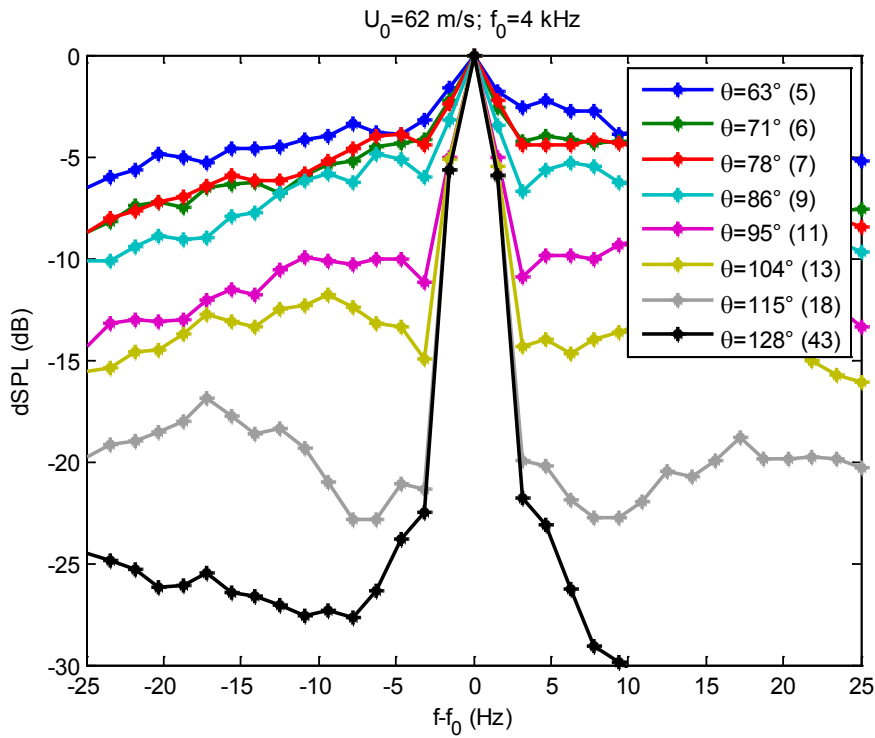


Figure 16: Zoom of Figure 13, showing individual frequency bands.

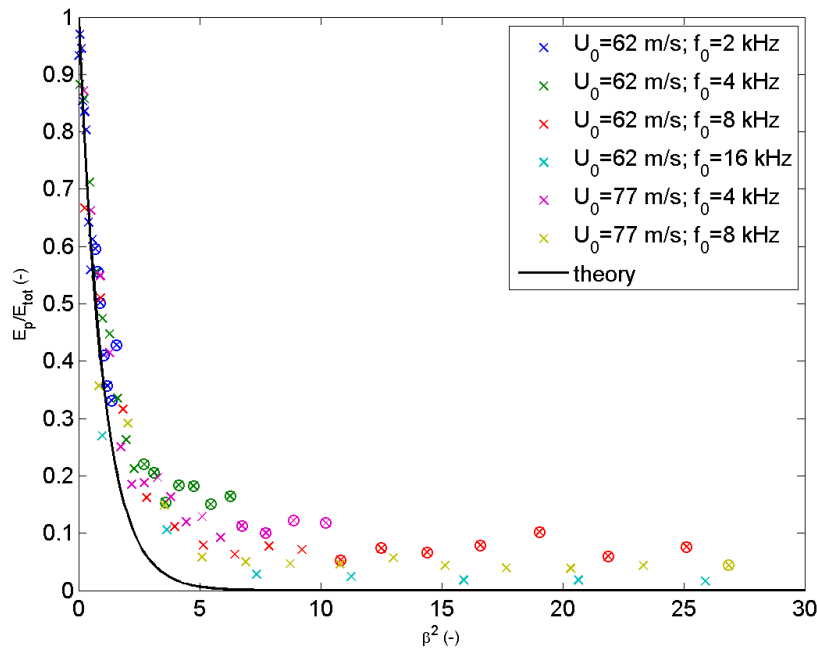


Figure 17: Energy ratio in the DNW-LLF for all usable measurements. Each series contains data for the axial row of 16 microphones. The black line shows the theoretical curve from Eq. (29). The circles indicate the cases for which the estimated Δf is smaller than 8 Hz.

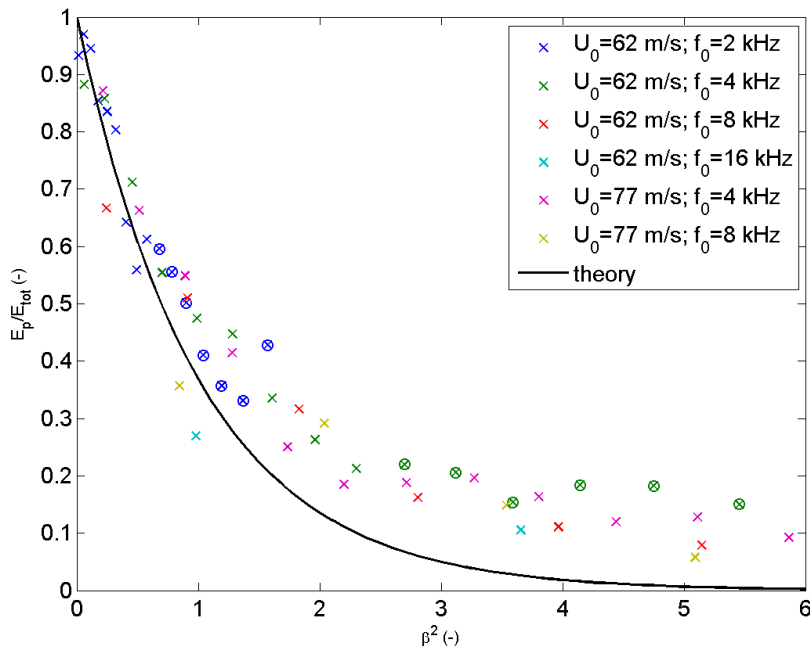


Figure 18: Zoom of Figure 17, showing results for small β .

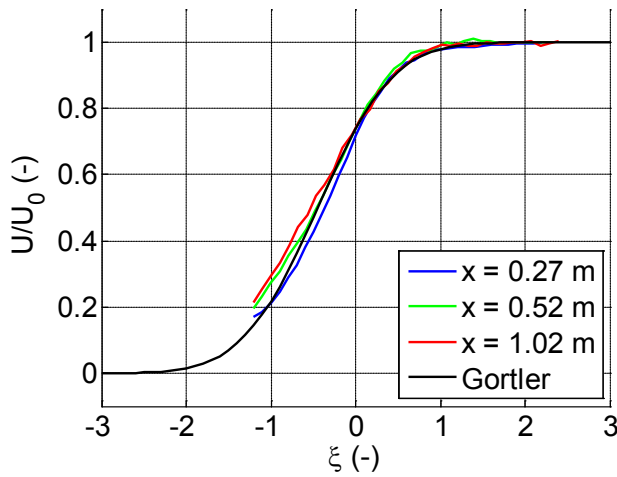


Figure 19: Normalised mean axial velocity profiles in KAT at 60 m/s. The black line shows the Görtler solution from Eq. (9) with $\sigma=9$.

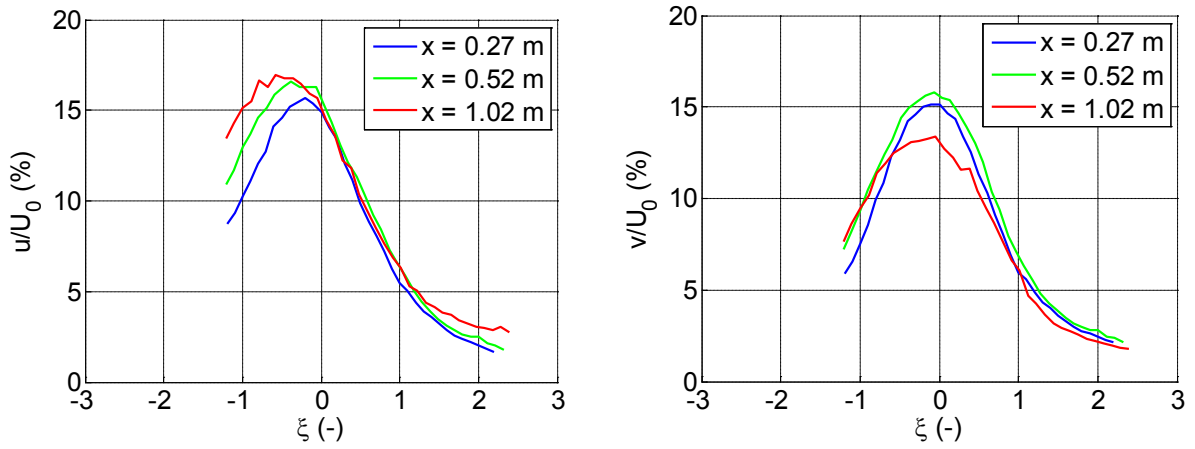


Figure 20: Axial (left) and lateral (right) turbulence intensity profiles in KAT at 60 m/s.

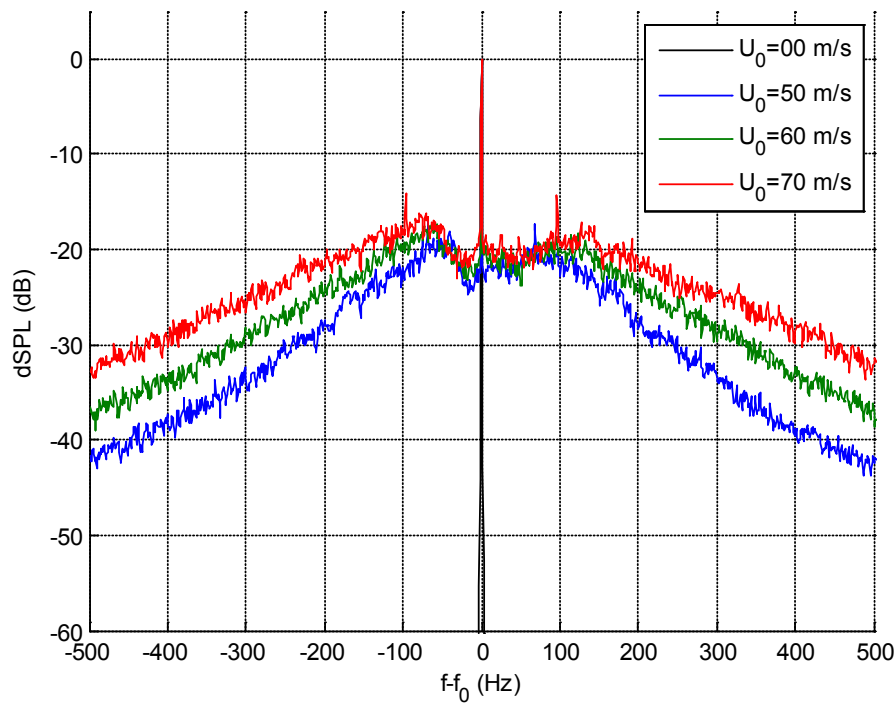


Figure 21: Effect of wind speed on spectral broadening in KAT for $x_s=x_m=1.02$ m and $f_0=4$ kHz.

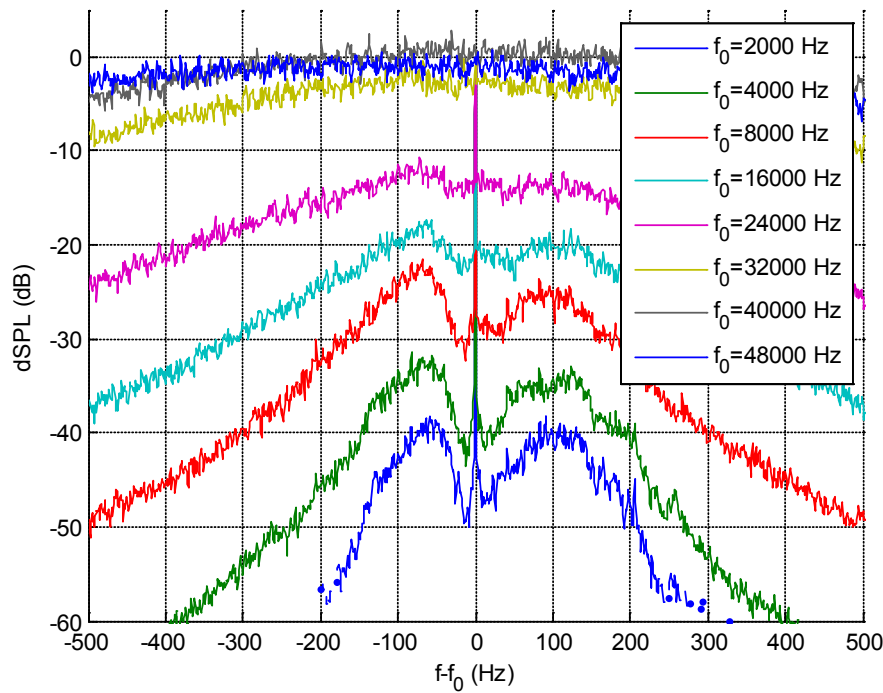


Figure 22: Effect of source frequency on spectral broadening in KAT for $x_s=x_m=0.52$ m and $U_0=60$ m/s.

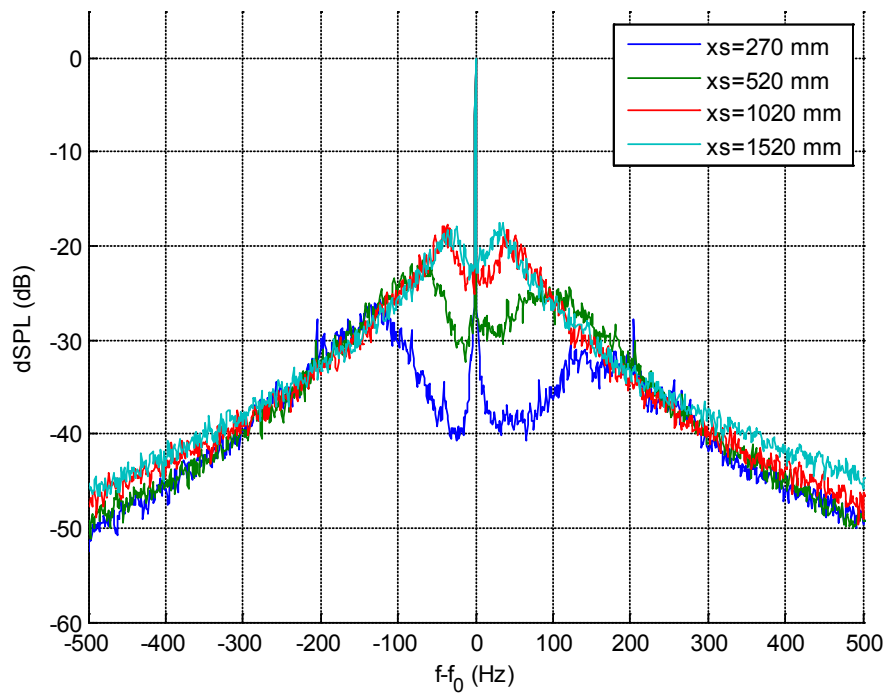


Figure 23: Effect of shear layer thickness on spectral broadening in KAT for $f_0=8$ kHz, $x_m=x_s$ and $U_0=60$ m/s.

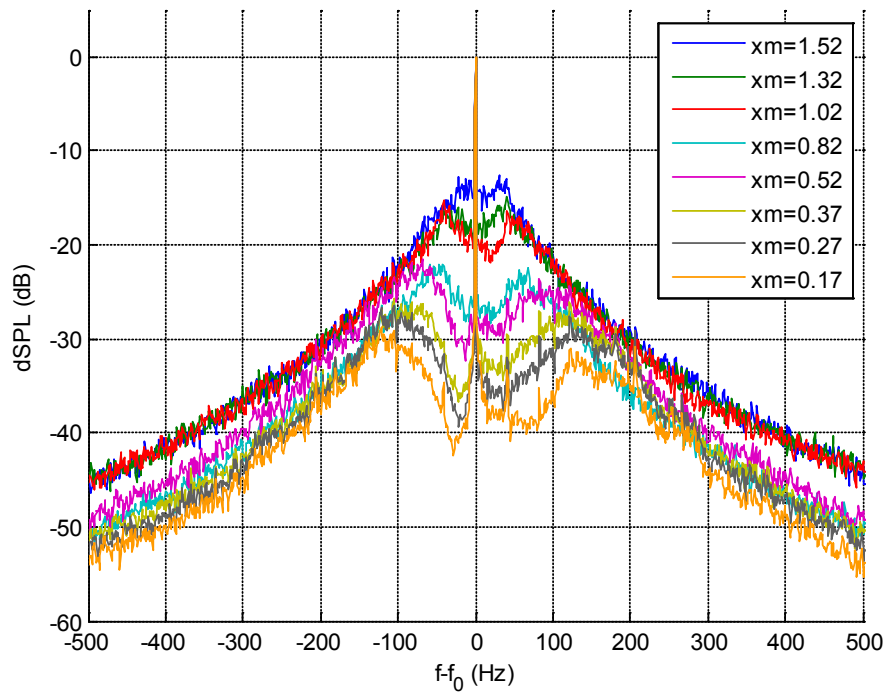


Figure 24: Effect of microphone position on spectral broadening in KAT for $x_s=0.52$ m, $f_0=8$ kHz and $U_0=60$ m/s.

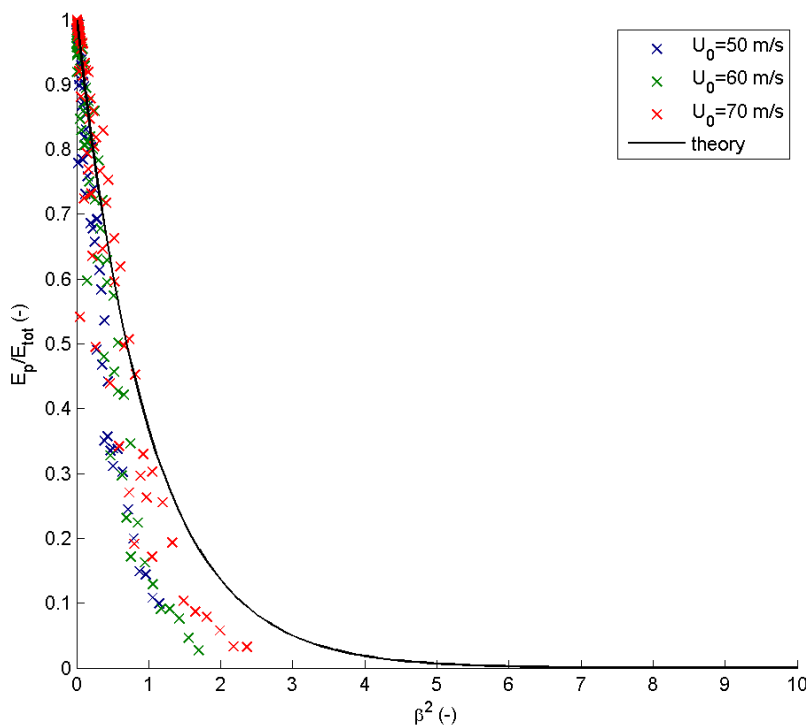


Figure 25: Energy ratio for $x_s=0.27$ m (KAT). Each series contains data for 5 frequencies and 16 microphones ($57^\circ < \theta < 108^\circ$). The black line shows the theoretical curve from Eq. (29).

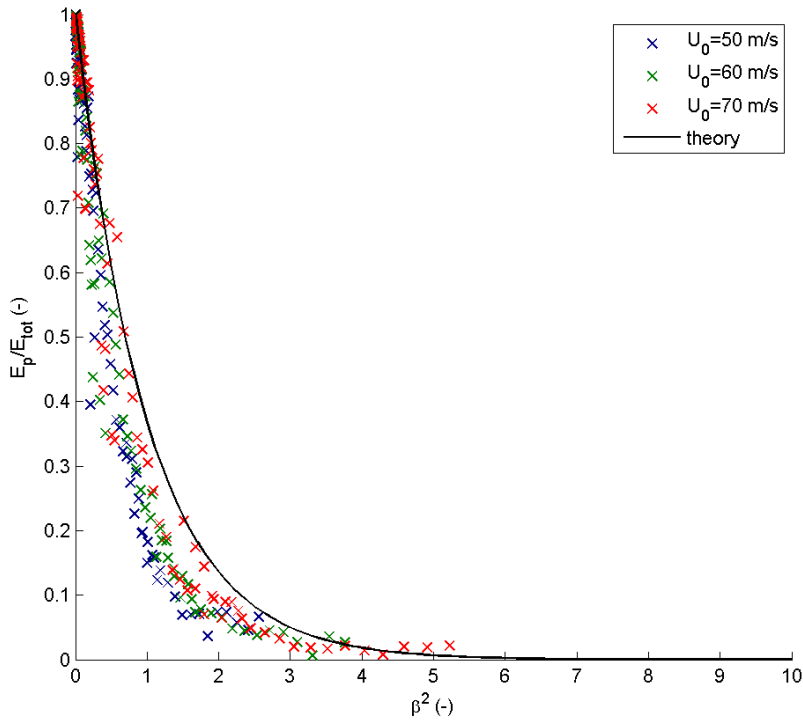


Figure 26: Energy ratio for $x_s = 0.52$ m (KAT). Each series contains data for 5 frequencies and 18 microphones ($57^\circ < \theta < 115^\circ$). The black line shows the theoretical curve from Eq. (29).

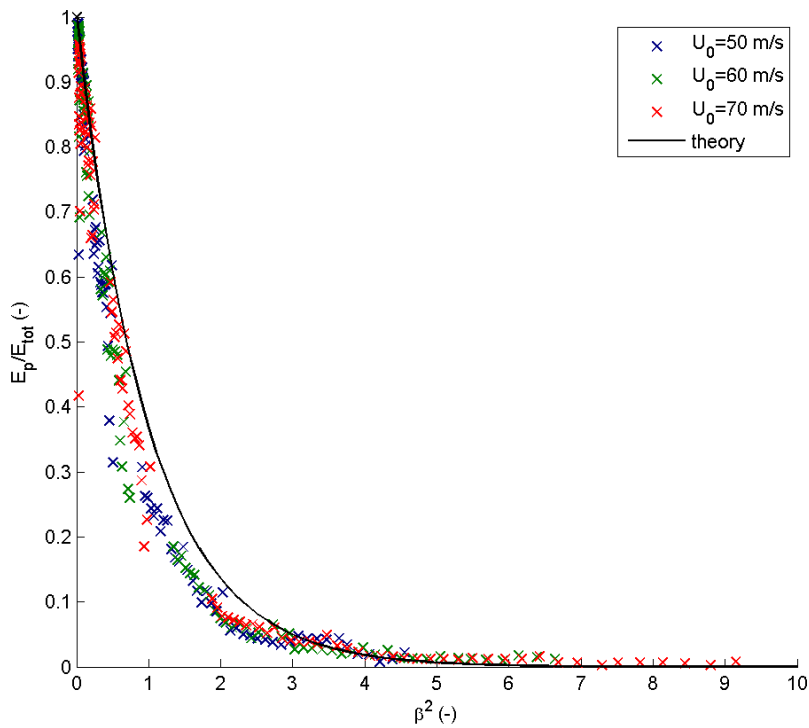


Figure 27: Energy ratio for $x_s = 1.02$ m (KAT). Each series contains data for 5 frequencies and 21 microphones ($57^\circ < \theta < 123^\circ$). The black line shows the theoretical curve from Eq. (29).

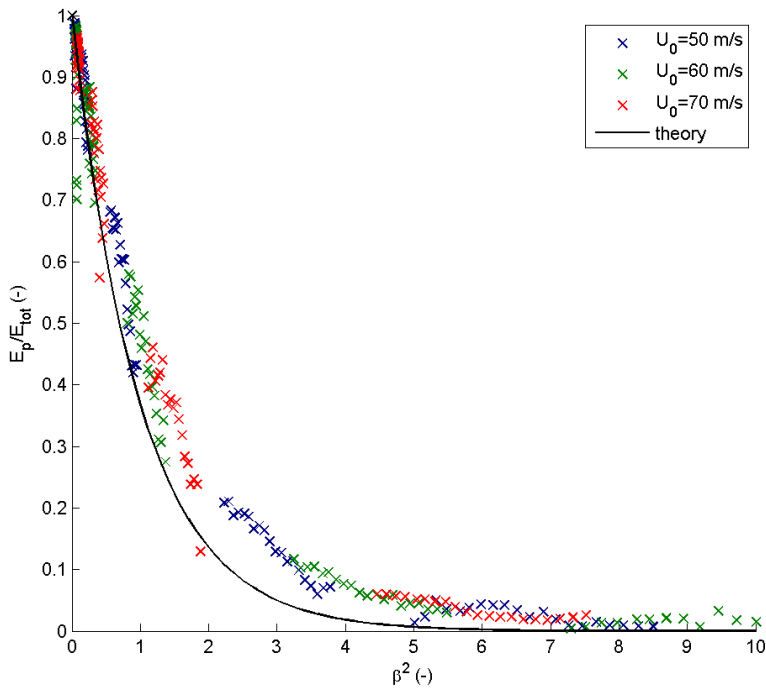


Figure 28: Energy ratio for $x_s = 1.52$ m (KAT). Each series contains data for 5 frequencies and 20 microphones ($60^\circ < \theta < 123^\circ$). The black line shows the theoretical curve from Eq. (29).

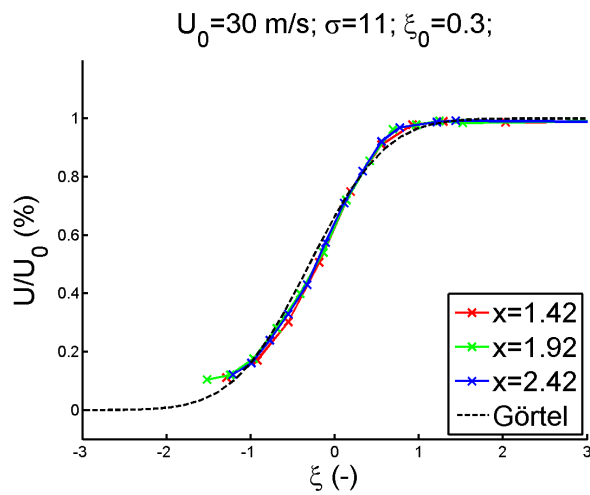


Figure 29: Normalised mean axial velocity profiles in DNW-NWB at 30 m/s. The black line shows the Görtler solution from Eq. (9) with $\sigma = 11$.

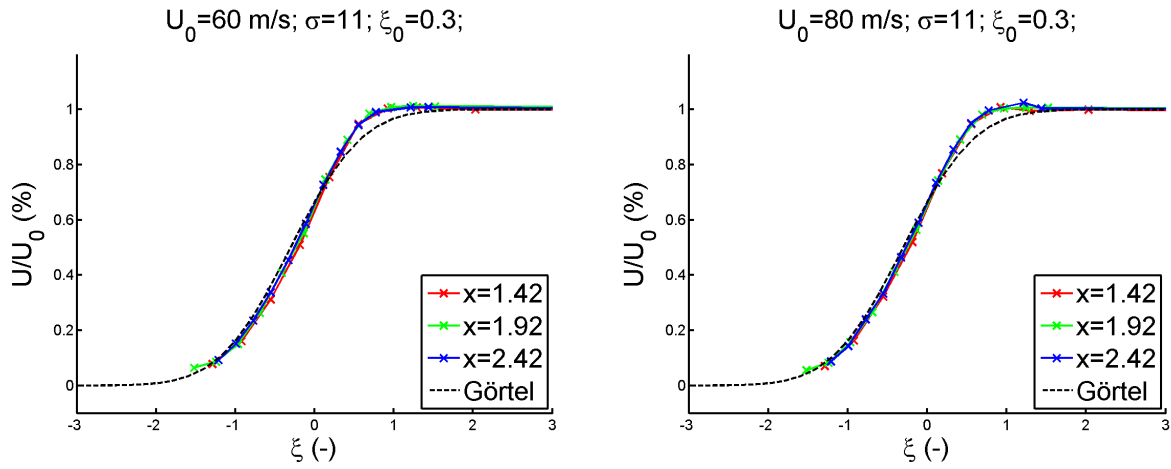


Figure 30: Normalised mean axial velocity in DNW-NWB at 60 m/s (left) and 80 m/s (right). The black line shows the Görtel solution from Eq. (9) with $\sigma=11$.

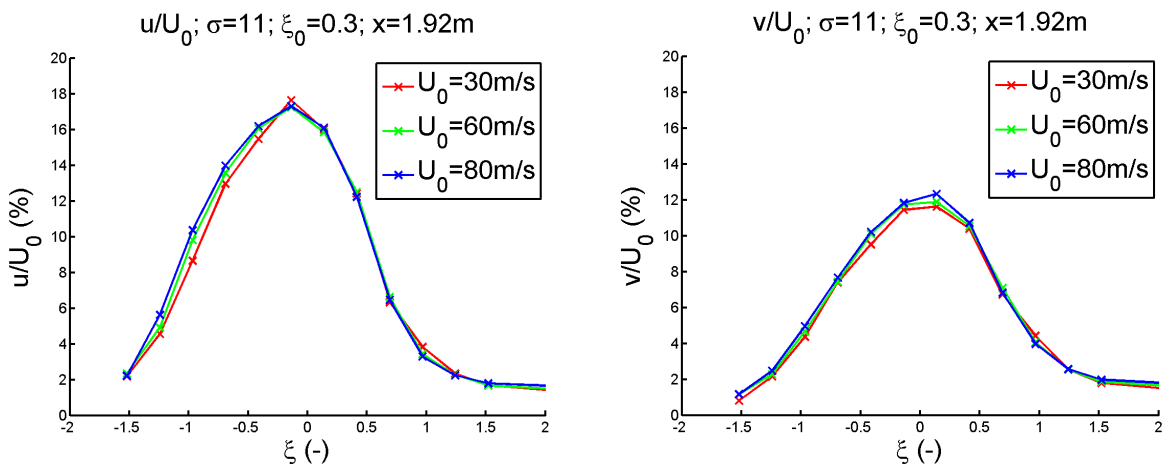


Figure 31: Axial (left) and lateral (right) turbulence intensity profiles in DNW-NWB at 30 m/s, 60 m/s and 80 m/s.

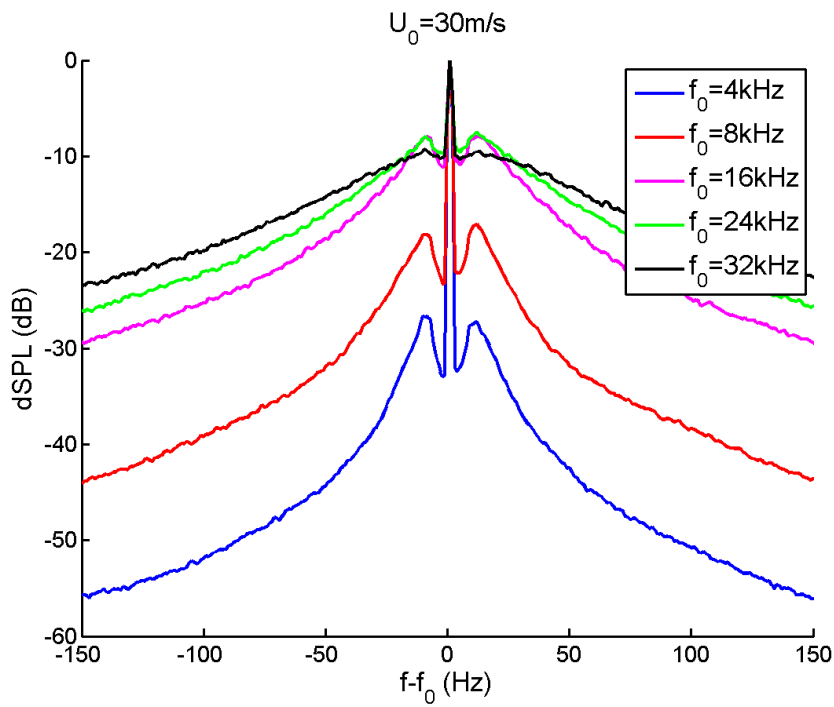


Figure 32: Effect of source frequency on spectral broadening in DNW-NWB and $U_0=30$ m/s.

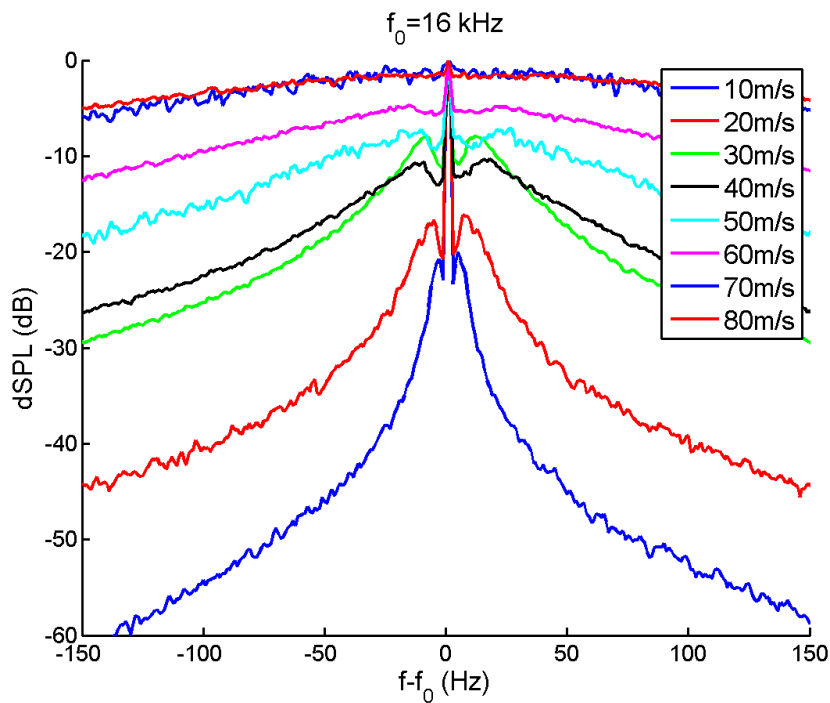


Figure 33: Effect of wind speed on spectral broadening in DNW-NWB and $f_0=16$ kHz.

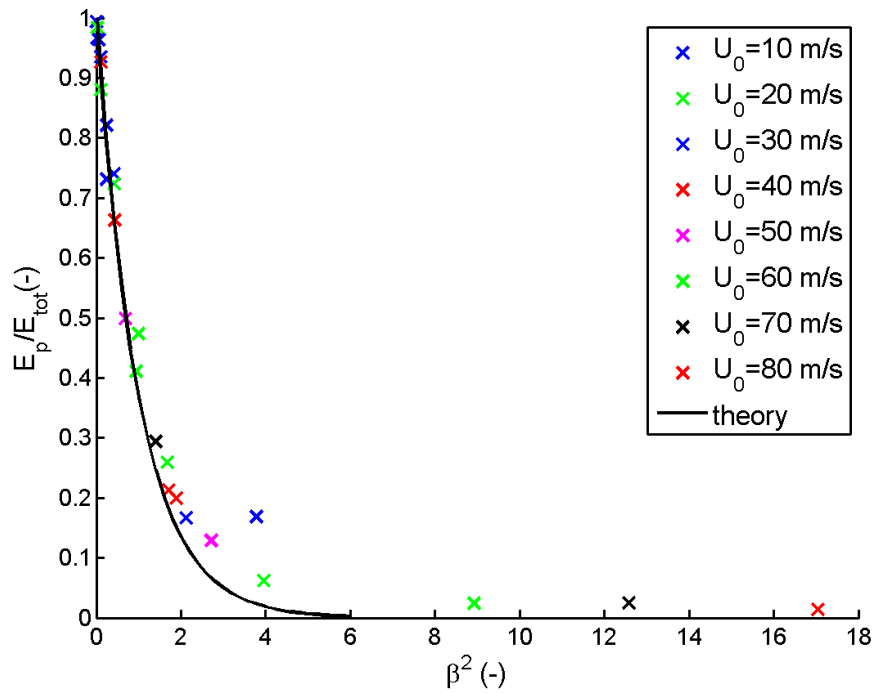


Figure 34: Energy ratio for $x_s = 1.92$ m in DNW-NWB. Each series contains data for 5 frequencies. The black line shows the theoretical curve from Eq. (29).